International Journal of Heat and Mass Transfer 251 (2025) 127388

Contents lists available at ScienceDirect

International Journal of Heat and Mass Transfer

journal homepage: www.elsevier.com/locate/ijhmt

Flow boiling heat transfer in a single microchannel and comparison with correlations

Joseph J. Widgington, Atanas Ivanov, Tassos G. Karayiannis *

Department of Mechanical and Aerospace Engineering, Brunel University of London, Uxbridge, UB83PH, UK

ARTICLE INFO

Keywords:
Microscale
Flow boiling
Heat transfer
Flow patterns
Correlations

ABSTRACT

The current research aimed to investigate the dominant heat transfer mechanisms during flow boiling of HFE-7100 in a single copper microchannel and use the data to assess predictive methods for the heat transfer coefficient. The single microchannel had a height of 0.811 mm, a width of 0.753 mm and a length of 75 mm, providing a hydraulic diameter of 0.7807 mm. Mass fluxes between 100 kg/m^{2}s and 1000 kg/m2s were investigated for heat fluxes up to 204.74 kW/m^2 at a constant inlet subcooling of 10 K. The inlet pressure was varied from 1, 1.5 and 2 bar. Four generic flow patterns were identified, namely: bubbly, slug, churn and annular flows, using a high-speed, high-resolution camera mounted on a microscope. Nucleate boiling was found to persist to some degree in all flow regimes. The effect of heat flux, mass flux and vapour quality on the two-phase heat transfer coefficient were considered and presented. The results were compared to existing heat transfer correlations.

1. Introduction

Flow boiling in microchannels has many potential applications due to possible high heat transfer rates that are a consequence of the large heat transfer surface area to flow area ratios and the utilisation of latent heat [1]. These applications extend to microelectronics cooling [2], photovoltaic thermal management [3], cooling of power electronics components and high-energy physics particle detectors [4]. The wide adoption of microscale flow boiling in industry is dependent on the ability to predict heat transfer rates and the consequent wall temperatures, such that micro heat exchangers can be sized accordingly. Similarly, the reliable prediction of the flow boiling pressure drop is essential for thermal engineers to estimate the pumping power required by the thermal management system that includes microscale heat exchangers. Both the above, i.e. heat transfer rates and two-phase pressure drop depend on the prevailing flow regimes in microchannels and a proper understanding of these patterns is a necessary starting point. This study aims to investigate microscale flow boiling heat transfer phenomena of HFE-7100, including the prevailing flow patterns and the accuracy of existing predictive models.

As previously mentioned, the understanding of heat transfer flow boiling phenomena is dependent on the resultant flow patterns. Thus, it is essential to first understand the resultant flow patterns in the microscale and how they differ from the conventional scale. The flow boiling regimes observed in conventional scale passages vary depending on the orientation of the flow. The most frequently encountered flow patterns in vertical flows at the conventional scale are bubbly flows, slug or plug flows, annular flows, wispy annular and mist flows, see Hewitt [5]. Flow patterns that occur during horizontal flows in the conventional scale, as classified by Hewitt and Roberts [6,7], are bubbly flows, stratified and wavy stratified flows, slug and plug flows, annular flows and mist flows. Some researchers include the term “intermittent flows”, as in Taitel [8], which has been subject to varied interpretations in the literature, even within the context of the conventional scale. In references [9–12] the term is used to describe flow patterns seen between bubbly and annular flows, such as slug, plug, and churn flows. Others [13–15] apply the term more narrowly, referring exclusively to slug or plug flows, excluding churn flow. However, further clarification on the term “intermittent flows” will be provided where relevant throughout the subsequent discussion.

Flow boiling patterns in the microscale are found not to be as dependant on flow orientation due to the suppression of the buoyancy force that occurs as a result of the smaller geometry. This effect is evidenced by the flow pattern categorisations utilised by researchers for both vertical and horizontal microscale flows. For example, Mahmoud

* Correspondence to: Tassos G. Karayiannis, Department of Mechanical and Aerospace Engineering, Brunel University of London, Uxbridge, Middlesex, UB8 3PH, UK.

E-mail address: tassos.karayiannis@brunel.ac.uk (T.G. Karayiannis).

https://doi.org/10.1016/j.ijheatmasstransfer.2025.127388
Received 2 April 2025; Received in revised form 31 May 2025; Accepted 5 June 2025
Available online 11 June 2025

Nomenclature

c_p	Specific Heat at Constant Pressure [J/(kgK)]
f_{sp}	Fanning Friction Factor [-]
g	Gravitational Acceleration [m/s^2]
h	Heat Transfer Coefficient [W/m^{2}K]
i	Enthalpy [J/kg]
i_{fg}	Latent Heat of Vapourisation [J/kg]
k	Thermal Conductivity [W/mK]
$\dot{m}$	Mass flow rate [kg/s]
n	Asymptotic Index [-]
r_c	Critical Cavity Radius [m]
r_{90}	Radius of 90° Bend [m]
q''	Heat Flux [W/m^2]
x	Vapour Quality [-]
y	Vertical Distance [m]
z	Distance from Channel Inlet [m]
A	Area [m^2]
Bd	Bond Number [-], $Bd = (\rho_l - \rho_g)gD_h{}^2/\sigma$
Bo	Boiling Number [-], $Bo = q''/(G{\cdot}h_{fg})$
C_o	Confinement Number [-], $C_o = 1/D_h\sqrt{\sigma/[g(\rho_l - \rho_g)]}$
D_h	Hydraulic Diameter [m]
E	Enhancement Factor [-]
Fr	Froude Number [-], $Fr = G/\rho\sqrt{(G{\cdot}D_h)}$
Fr_{lo}	Liquid only Froude Number [-], $Fr = G/\rho_l\sqrt{(G{\cdot}D_h)}$
G	Mass Flux [kg/m^{2}s]
H	Height [m]
K	Pressure Loss Coefficient [-]
L	Length [m]
L_e	Hydrodynamic Entry Length [m]
M	Molecular Weight [g/mol]
N_{co}	Convection Number [-], $N_{co} = [(1-x)/x]^{0.8}\sqrt{\rho_g/\rho_l}$
Nu	Nusselt Number [-], $Nu = hD_h/k$
P	Pressure [Pa]
P_R	Critical Pressure [Pa]
Pr	Prandtl Number [-], $Pr = \mu C_p/k$
Q	Heating [W]
Rp	Roughness Profile Parameter [-],
Re	Reynolds Number [-], $Re = GD_h/\mu$
Re_{gs}	Gas Reynolds Number [-], $Re_{gs} = GxD_h/\mu_g$
Re_{lo}	Liquid Only Reynolds Number [-], $Re_{lo} = GD_h/\mu_l$
Re_{ls}	Liquid Reynolds Number [-], $Re_{ls} = G(1-x)D_h/\mu_l$
T	Temperature [K]
W	Width [m]
We	Weber Number [-], $We = G^2D_h/(\rho{\cdot}\mu)$
We_{go}	Gas Only Weber Number [-], $We_{go} = G^2D_h/\left(\rho_g{\cdot}\mu_g\right)$
We_{lo}	Liquid Only Weber Number [-], $We_{lo} = G^2D_h/(\rho_l{\cdot}\mu_l)$
$\varnothing_{pl}$	Plenum Diameter [m]

Greek

α	Aspect Ratio [-], $\alpha = H_{ch}/W_{ch}$
α^*	Adjusted Aspect Ratio [-], $\alpha^* = \max(H_{ch}/W_{ch},\ W_{ch}/H_{ch})$
δ_{th}	Thermal Boundary Layer Thickness [m]
ΔP	Pressure Drop [Pa]
ΔT	Temperature Difference [K]
μ	Viscosity [Pa•s]
ν	Specific Volume [m^3/kg]
ρ	Density [kg/m^3]
σ	Surface Tension [N/m]
φ	Bubble to Wall Contact Angle [rad]
χ	Martinelli Parameter [-], $\chi = \left[(dP/dz)_l/(dP/dz)_g\right]^{0.5}$

Subscripts

b	Base
cb	Convective Boiling
ch	Channel
col	Column
cu	Copper
f	Fluid
FD	Fully Developed
g	Vapour
in	Channel Inlet
l	Liquid
$meas$	Measured
mod	Modified
nb	Nucleate Boiling
out	Channel Outlet
pl	Plenum
sat	Saturation
sc	Sudden Contraction
se	Sudden Expansion
sub	Subcooled
sup	Superheat
sp	Single-phase
tp	Two-phase
ts	Top Surface
w	Wall
∞	Ambient
3	Adjusted for 3 Sides
90	90° Change in Direction

and Karayiannis [16] investigated flow boiling in vertical mini-tubes and utilised the generic categorisations of bubbly, slug, churn and annular flows. They went on to recommend correlations for the transition boundaries between these four generic flow regimes. Al-Zaidi et al. [17] investigated the flow boiling of HFE-7100 in a horizontal microchannel heat sink and also utilised the generic categorisations of bubbly, slug, churn and annular flows. The interfacial geometry, i.e. the resultant structure at the liquid-vapour boundary, that occurs during these flow patterns plays a key role in heat transfer rates and pressure drop that occurs during flow boiling.

The interfacial structures that arise between the two phases significantly affect heat transfer and pressure drop as they present different heat transfer and pressure drop mechanisms. For example, a main driver of heat transfer during bubbly flow is the agitation of the bulk fluid as bubbles depart the surface [18]. This cannot occur if bubble nucleation is suppressed, as it can be during some annular flows. Conversely, heat transfer rates can be increased during annular flow by thinning of the liquid film, which is not present during bubbly flows. With regards to pressure drop, flow can almost be considered homogeneous during dispersed bubbly flow, a flow pattern where small bubbles are suspended in the liquid with a velocity equal to that of the bulk liquid. Here there is not slippage or shear between phases [7]. Conversely, during annular flows there is a significant difference in phase velocities and significant shear occurs at the phase interface, thus greatly affecting the pressure drop through an entirely different mechanism.

Understanding the distinct aforementioned mechanisms is essential for developing accurate predictive models. The present study focuses on the prediction of the heat transfer coefficients in microchannels, with

the prediction of pressure drop being outside the scope of this paper. The current methodologies for heat transfer prediction for flow boiling in both conventional sized and microscale channels can be separated into four classifications [19]:

(i) Superposition models, in which the two-phase heat transfer coefficient (h_{tp}) includes the individual components of the nucleate boiling (h_{nb}) and convective boiling heat transfer mechanisms (h_{cb}). An example of this is the correlation proposed by Chen [20] for conventionally sized vertical tubes. The form of the superposition models is shown in Eq. (1).

$$h_{tp} = h_{nb} + h_{cb} \tag{1}$$

(ii) Enhancement models, where the two-phase heat transfer coefficient is considered as an enhancement of the single-phase heat transfer coefficient (h_{sp}), with an empirical enhancement factor (E). One example is the correlation suggested by Lee and Mudawar [21]. The enhancement model form is presented below in Eq. (2).

$$h_{tp} = Eh_{sp} \tag{2}$$

(iii) Asymptotic models, which provide a similar form to the superposition models with the exception of an asymptotic index (n), as displayed in Eq. (3). A notable example is the correlation introduced by Kim and Mudawar [22].

$$h_{tp}{}^{n} = h_{nb}{}^{n} + h_{cb}{}^{n} \tag{3}$$

(iv) Dimensionless models, where the two-phase heat transfer coefficient is predicted as a function of various dimensionless groups, commonly developed from empirical fits of data as follows:

$$h_{tp} = f(Bo,\ Re,\ Bd,\ We,\ \chi, \ldots,\ \ldots)\frac{k_l}{D_h} \tag{4}$$

The use of dimensionless models is particularly common, with the most recent example of this provided by Zhang et al. [23]. The dimensionless groups of Eq. (4) are given in the Nomenclature section.

The superposition models and the asymptotic models require consideration of the nucleate boiling and convective boiling heat transfer mechanisms. The nucleate boiling mechanism is dependent on bubble nucleation and, as is true in pool boiling and flow boiling, heat transfer coefficients increase with larger heat fluxes due to larger bubble departure diameters, higher bubble generation frequency and an increase in active nucleation sites [24,25]. The increase in bubble generation frequency and nucleation site density results in agitation and greater mixing of the bulk fluid. Consequently, heat transfer coefficients are dominated by the effect of heat flux during the nucleate boiling regime, with minimal dependency on the mass flux effect.

The convective boiling mechanism is said to be dominated by the characteristics of the liquid film, which occurs in some intermittent and, particularly, in annular flows [26]. The term intermittent here refers to the inclusion of slug, plug and churn flows. Heat transfer coefficients are significantly affected by mass flux and vapour quality due to the reduction of the liquid film thickness. The reduction in film thickness causes a lower thermal resistance and a subsequent enhancement of evaporation from the film to the core [27]. In consequence, heat transfer coefficients are predominantly affected by the role of mass flux, with little to no reliance on the heat flux [28].

There remains disagreement amongst researchers as to the dominant flow boiling heat transfer mechanisms in microchannels, with some researchers arguing that nucleate boiling dominates, [29,30] or is evident in all flow regimes, [17], other researchers [31,32] reporting that the convective boiling mechanism dominates and a third group [21,33–35] proposing that nucleate boiling dominates at low heat fluxes and convective boiling dominates at higher heat fluxes, with a mixture of the two mechanisms at intermediate heat fluxes. The lack of agreement regarding the dominant heat transfer mechanisms has resulted in significant difficulty in fully capturing certain parametric effects such as wall heat flux and mass flux, when developing correlations. Therefore, correlations are currently mostly only applicable to a specific fluid and operating conditions [1].

This study seeks to report and explain the heat transfer characteristics for newly obtained experimental data for HFE-7100 in a single microchannel and to compare these data with existing heat transfer correlations. The objectives of the present study are to help enhance the understanding of the predictive behaviour of these correlations by examining the heat transfer mechanisms and directly relating them to flow patterns observed through high-speed, high-resolution flow visualisation. This includes understanding the role of mass flux, heat flux and system pressure on heat transfer coefficients for HFE-7100.

2. Experimental methodology

2.1. Experimental flow loops

A schematic diagram of the experimental facility is depicted in Fig. 1. It consisted of a main closed flow loop and a separate auxiliary cooling loop (dotted blue line). The electrical connections are also represented in the schematic (dotted red line). A photograph of the facility is displayed in Fig. 2. The main closed flow loop consisted of a 9 L reservoir tank, a brazed plate heat exchanger sub-cooler, a Tuthill micro gear pump (controlled by a phase inverter drive), a Krohne Optimass Coriolis flow meter, filter, sight glass, test section and brazed plate heat exchanger condenser. The reservoir was wrapped in a tape heater and fitted with a reflux condenser tube, attached to the reservoir venting valve. The inlet pipe work was also wrapped in tape heaters and insulation to achieve the desired level of sub-cooling. A gas-loaded hydraulic accumulator was added to the system to eliminate undesirable pressure fluctuations and a flexi hose to remove undesired noise from the Coriolis flow meter.

Heating of the reservoir was used to both degas the fluid through vigorous boiling and to adjust the system pressure of the system. The sub-cooler was installed prior to the pump to ensure full condensation of the fluid before entering the pump inlet, thus avoiding cavitation. A brazed plate heat exchanger was placed after the test section to condense the fluid entering the fluid reservoir. The reservoir tank tape heater and preheater were controlled using two, individual Variacs. The test section heater cartridges were controlled using a high voltage variable DC power supply.

A water chiller was used to reject heat from the main closed flow loop, capable of providing up to 14 L/min of water-glycol mixture with outlet temperatures between 8°C and 35°C at a total cooling capacity of 7 kW. The secondary loop provided cold side flows to the brazed plate condenser and sub-cooler. All instrument measurements, i.e. pressure transducer measurements, thermocouple measurements and mass flow rates, were collected using a National Instruments Data Acquisition System (DAQ) at a frequency of 1 kHz. Flow visualization was conducted using a Phantom MiroLab 110 high-speed, high resolution digital camera at 6000 fps with a resolution of 512×512 pixels. A Huvitz HSZ-645TR microscope and LED lighting system were used in conjunction with the high-speed camera to facilitate flow visualisation.

2.2. Test section

A rendered Computer Aided Design (CAD) exploded view of the test section assembly is presented in Fig. 3. The test section assembly consisted of four main component groups, namely: the aluminium clamping

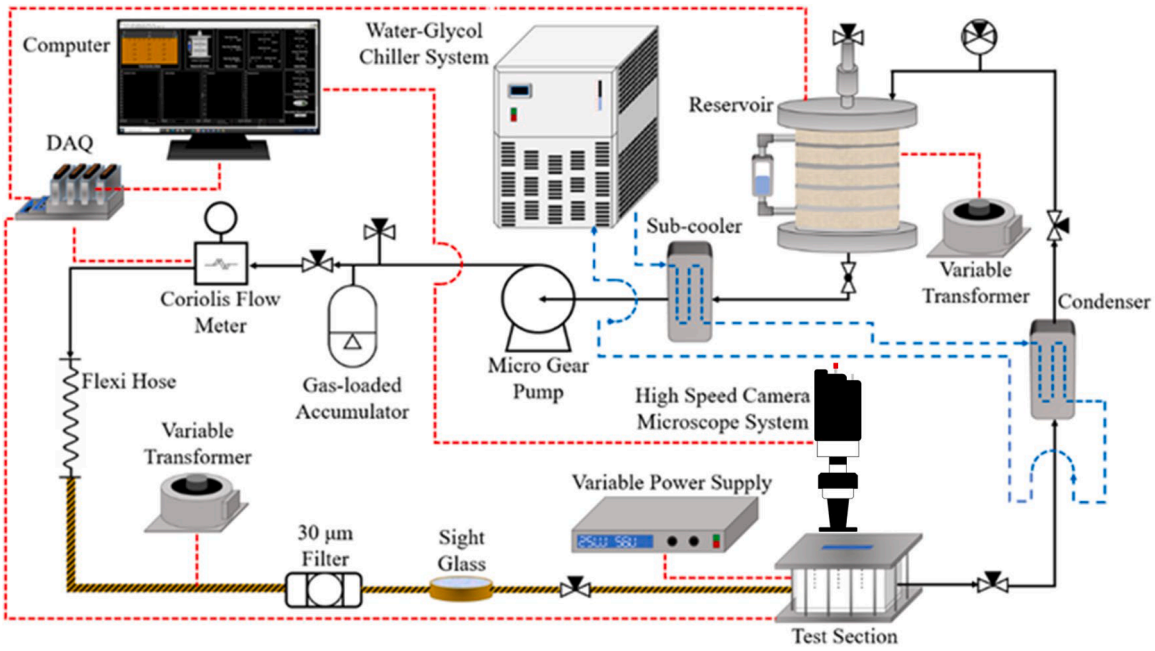

Fig. 1. Schematic diagram of the experimental facility.

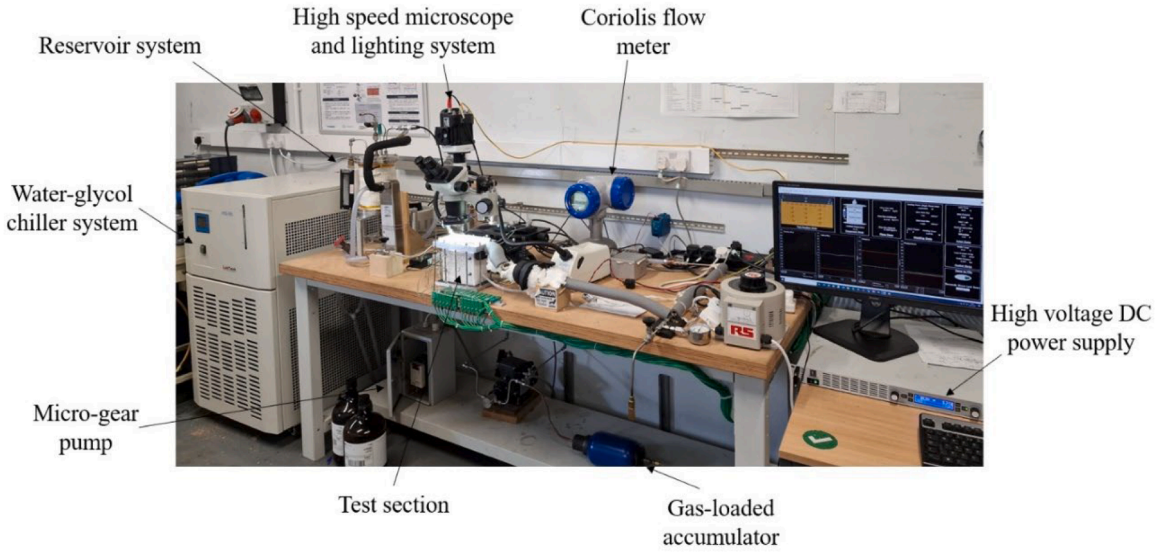

Fig. 2. Experimental facility.

plates, the polytetrafluoroethylene (PTFE) housing, the clear polycarbonate viewing plate and the oxygen-free copper test section. The aluminium clamping plates were used to hold the microchannel copper block in place and prevent leakage from the microchannel. The PTFE housing was used to house the copper block, limit heat loss and provide a base for the cartridge heaters that were used to apply heat to the block. The housing was fabricated in three parts to assist in ease of manufacture. The housing components included the base housing, the front housing and the back housing, which were fastened together using four M5 bolts. Twenty-three 0.6 mm diameter holes were drilled into the front housing to pass thermocouple wires into the copper block. Flow was contained in the microchannel using a clear polycarbonate top viewing plate, which also permitted flow visualisation and subsequent categorisation of flow patterns. Two 1 mm diameter circular shaped plena were milled into the polycarbonate viewing plate, each with 3 holes drilled into the plena for flow inlet/outlets, temperature measurements and pressure measurements. A single cartridge heater was used to heat the test section with a total heating capability of 500 W.

Fig. 4 displays two rendered CAD drawings of the oxygen-free copper test section. It was designed with a total height of 95 mm, a base width of 84 mm and a base depth of 8 mm. A single 12.5 mm hole was drilled into the 20 mm wide base of the copper block to insert a 500 W cartridge heater. The microchannel, plena and o-ring groove were milled into the block using a Hurco VM1 CNC machine, with a 0.5 mm end mill at a rotation speed and feed rate of 8000 rpm and 200 mm/min, respectively. The inlet and outlet plena were formed of two 1 mm diameter circles, which aligned with the plena machined into the clear polycarbonate top plate. An o-ring groove was machined on the outer lip to prevent any leakage of the fluid or air entering the working fluid. The microchannel was designed with a square cross section of 0.75 mm and length of 74.15 mm. Measurements taken using a Zeiss O-Inspect 01–442 multi-sensor measurement machine found an average channel height, width and

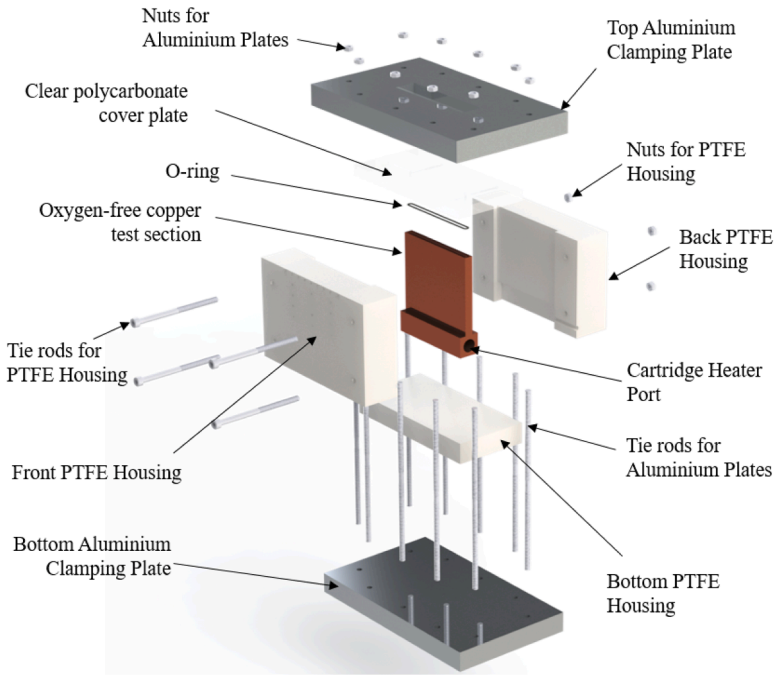

Fig. 3. Exploded CAD view of test section assembly.

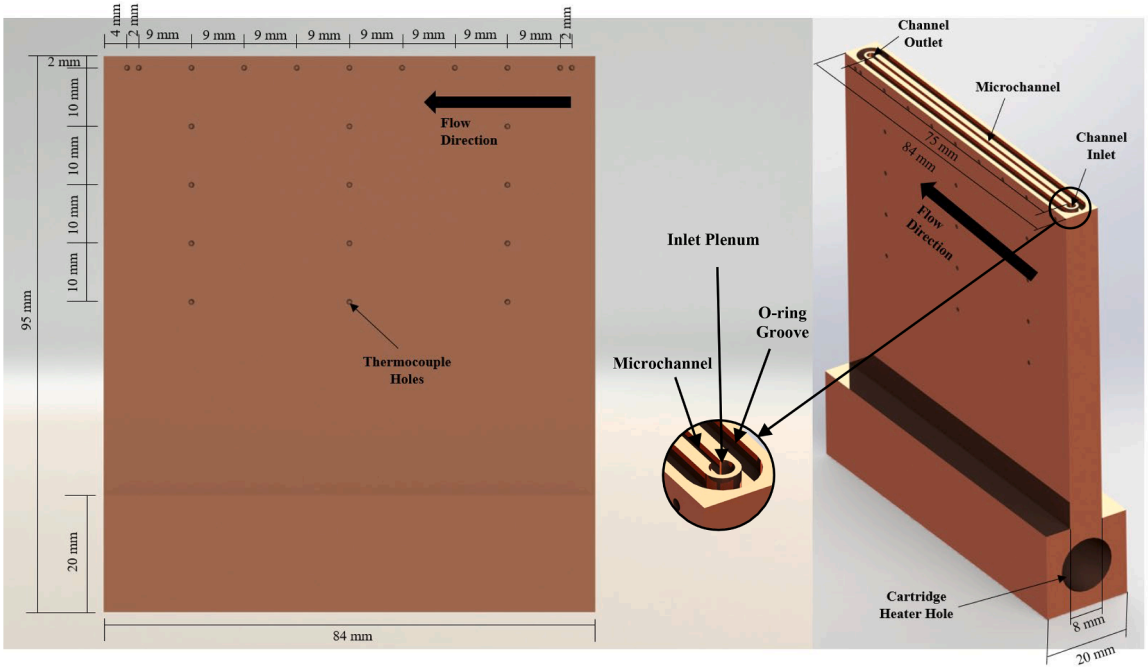

Fig. 4. Rendered CAD images of copper test section (left) front view with thermocouple hole diagram (right) isometric view with plena and microchannel.

length of 0.811 mm, 0.753 mm and 74.22 mm, respectively. These measured values were used in the data reduction presented in the following section. Twenty-three 0.6 mm diameter thermocouple holes were drilled into the front face of the copper base, at a depth of 4 mm in the arrangement shown in Fig. 4. This arrangement was developed to assess the temperature distribution along the channel as well as the vertical and horizontal heat flux in the copper base. The last row of thermocouples was located 1.2 mm below the surface of the channel.

A Bruker NP Flex 3D non-contact, white light optical profiling machine, located in the Precision Manufacturing Centre at The University of Nottingham, was used to measure the channel surface roughness parameters. The average surface roughness, Ra, was 0.168 μm, while the area surface roughness, Sa was 0.172 μm.

Flow boiling was investigated for mass fluxes between 100 kg/m^{2}s and 1000 kg/m^{2}s for channel inlet pressures of 1 bar, 1.5 bar and 2 bar at channel wall heat fluxes up to 204.74 kW/m^2. The properties for HFE-7100 at the three used inlet pressures are displayed in Table 1. The percentage change between the thermophysical properties at 1 bar and 2 bar are also included in the table, which may provide further insight into the mechanisms that cause any differences between heat transfer results at higher system pressures. The most significant and noticeable changes to the thermophysical properties include an increase to the vapour-

Table 1
Thermophysical properties of HFE-7100.

Inlet Pressure (bar)	T_{sat} (°C)	ρ_l (kg/m^3)	ρ_g (kg/m^3)	i_{fg} (kJ/kg)	$C_{p,l}$ (kJ/kg•K)	$C_{p,g}$ (kJ/kg•K)	μ_l (μPa•s)	μ_g (μPa•s)	k_l (W/m•K)	k_g (W/m•K)	σ (N/m)
1	60.67	1420	9.52	116	1.19	0.925	393.7	19.84	0.06185	0.00859	0.0096
1.5	73.35	1383	14.03	112	1.21	0.954	341.6	20.61	0.05938	0.00920	0.0085
2	83.08	1353	18.53	109	1.23	0.976	312.2	21.22	0.05748	0.00983	0.0077
% Diff.	–	**-4.7 %**	**94.6 %**	**-6.0 %**	**3.4 %**	**5.5 %**	**-20.7 %**	**7.0 %**	**-7.1 %**	**14.4 %**	**-19.8 %**

phase density of 94.6 %, a reduction in the viscosity of the liquid-phase of 20.7 % and a decrease of the surface tension by -19.8 %. A constant channel inlet subcooling of 10 K was used for all experiments.

2.3. Data reduction

A linear relationship was obtained between the temperatures recorded by each of the three columns of thermocouples in the test section and the distance from the bottom surface of the microchannel, see Fig. 4. This was then differentiated to give the temperature gradient in the block and the heat flux for each column, q''_{col}, as follows:

$$q''_{col} = -k_{cu}\left.\frac{dT_{col}}{dy}\right|_{y=0} \tag{5}$$

where k_{cu}, T and y are the thermal conductivity of copper, temperature and vertical length dimension, respectively.

The difference in the heat flux calculated for the three thermocouple columns was found to be no greater than 6.7 % for all collected data points and consequently, a one-dimensional heat flux in the vertical direction was assumed as the arithmetic mean of three column heat flux values, i.e.

$$q''_b = \frac{q''_{col\ 1} + q''_{col\ 2} + q''_{col\ 3}}{3} \tag{6}$$

The channel wall heat flux, q''_w, was then calculated using the calculated base heat flux with a uniform channel and plenum heat flux as follows:

$$q''_w = \frac{q''_b A_b - Q_{top}}{(2H_{ch} + W_{ch})L_{ch} + A_{pl_{heat}}} \tag{7}$$

where A_b, $A_{pl_{heat}}$, Q_{loss}, H_{ch}, W_{ch} and L_{ch} are the copper base cross-sectional area, the total heated plena area, the heat loss through the top plate, the channel wall height, the channel base width and the length of the channel, respectively. The heat loss through the top plate was calculated by finding the heat transfer coefficient as a function of the difference between the external surface temperature of the test section top wall, T_{ts} and the ambient temperature T_∞ experimentally.

The microchannel was placed under vacuum conditions and low power heat was applied to the test section. Vacuum conditions were achieved by closing the valve downstream of the test section and attaching a vacuum pump to the test section inlet connection. The base heat flux was calculated as per Eq. (5) and Eq. (6) once steady state conditions were reached. It was then assumed that the power lost through the test-section top plate was equal to the product of the heat flux measured in the vertical direction and the base cross-sectional area, i.e.:

$$q''_b A_b = Q_{top} = h_{top}(T_{ts} - T_\infty) \tag{8}$$

where h_{top} is the overall heat transfer coefficient of heat lost to the top plate and is dependent on the difference between the test section top surface temperature and the ambient temperature. This relationship is shown in Fig. 5.

The mass flux, G, was calculated from the mass flow rate, $\dot{m}$, using the following equation:

$$G = \frac{\dot{m}}{H_{ch}W_{ch}} \tag{9}$$

For single-phase validation, the experimental Fanning friction factor, f_{sp}, was found from:

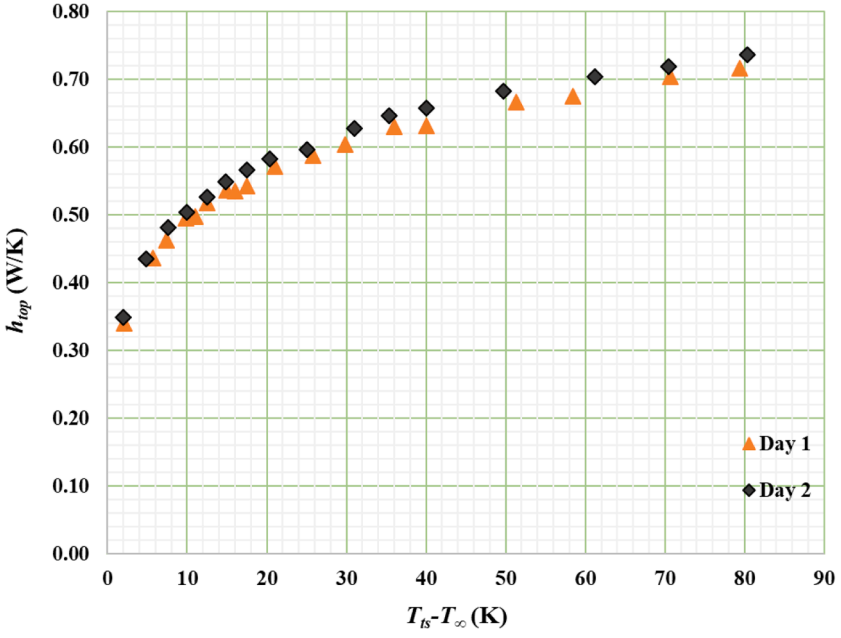

Fig. 5. Experimental heat transfer coefficient of heat loss from top plate.

$$f_{sp} = \frac{\Delta P_{ch} D_h \rho_f}{2 L_{ch} {G_{ch}}^2} \tag{10}$$

The pressure drop across the channel, ΔP_{ch}, was calculated differently for the single-phase and flow boiling experimental cases through consideration of pressure drops in the plenums. Note that the flow turns at 90° to enter the plenum and subsequently contracts to enter the microchannel. At the exit, the flow expands in the plenum and turns again by 90° to exit into the flow pipe. The pressure sensors are located at the inlet and exit pipes leading to the corresponding plena. The pressure drop was calculated as follows:

$$\Delta P_{ch} = \Delta P_{meas} - \left(\Delta P_{in,90} + \Delta P_{sc} + \Delta P_{se} + \Delta P_{out,90}\right) \tag{11}$$

where ΔP_{meas}, $\Delta P_{in,90}$, ΔP_{sc}, ΔP_{se} and $\Delta P_{out,90}$ are the measured pressure drop, the pressure drop due to a 90° bend in the manifold, the pressure drop due to a sudden contraction between the inlet plenum and the channel, the pressure drop due to a sudden expansion between the channel and the outlet plenum and the pressure drop due to a 90° bend in the outlet plenum, respectively. The single-phase plenum pressure drop components were calculated using the equations presented in Eq. (12) to Eq. (15), where Eq. (12) and Eq. (13) were proposed by Remsburg [36], whilst the pressure losses due to sudden expansions and contractions shown in Eq. (14) and Eq. (15) were proposed by Kays and London [37].

$$\Delta P_{in,90} = \frac{K_{90} {G_{pl}}^2}{2\rho_l} \tag{12}$$

$$\Delta P_{Out,90} = \frac{K_{90} {G_{pl}}^2}{2\rho_l} \tag{13}$$

$$\Delta P_{sc} = \frac{{G_{ch}}^2}{2\rho_l}\left[\left(1 - \left(\frac{A_{ch}}{A_{pl}}\right)^2\right) + K_{sc}\right] \tag{14}$$

$$\Delta P_{se} = \frac{{G_{ch}}^2}{2\rho_l}\left[\left(1 - \left(\frac{A_{ch}}{A_{pl}}\right)^{2^2}\right) + K_{se}\right] \tag{15}$$

K_{90} represents the loss coefficient for 90° changes in flow direction, which was proposed by Phillips [38] to be 1.2 and ρ_l represents the liquid density. K_{sc} and K_{se} represent the coefficients for a sudden contraction and a sudden expansion, respectively. These values were extracted from the figure provided by Kays and London and were found to be 1.133 for sudden contractions and 1.0 for sudden expansions.

As mentioned above, constant channel inlet subcooling of 10 K was used for all flow boiling experiments. Consequently, it was assumed that the channel inlet was single-phase liquid and hence, Eq. (12) and Eq. (13) were deemed suitable for estimating the pressure drop in the inlet plenum. However, two phase pressure drop components were considered for flow boiling experiments. The sudden expansion at the outlet of the microchannel into the plenum was calculated using Eq. (16), proposed by Markal et al. [39], taken from Blevins [40] and Collier and Thome [7].

$$\Delta P_{se} = \frac{v_l + x_{out}\left(v_g - v_l\right)}{2}\left[\left({G_{pl}}^2 - {G_{ch}}^2\right) + \left(1 - \frac{A_{ch}}{A_{pl}}\right){G_{ch}}^2\right] \tag{16}$$

The two-phase pressure drop due to the 90° bend of flow in the outlet plenum was calculated using Eq. (17) and Eq. (18), which were proposed by Chisholm [41], where r_{90} is the bend radius in the plenum and $\varnothing_p$ is the diameter of the plenum.

$$\Delta P_{Out,90} = \frac{{G_{ch}}^2 K_{90}}{2\rho_l}\left\{1 + \left[\left(\frac{\rho_l}{\rho_g} - 1\right)\left(Bx_{out} - B{x_{out}}^2 + {x_{out}}^2\right)\right]\right\} \tag{17}$$

$$B = 1 + \frac{2.2}{K_{90}\left(2 + \frac{r_{90}}{\varnothing_{pl}}\right)} \tag{18}$$

The local vapour quality was calculated using Eq. (19), where $i(z)$, $i_l(z)$ and $i_{fg}(z)$ represent the local specific enthalpy, the saturated liquid enthalpy and the enthalpy of vapourisation, respectively.

$$x(z) = \frac{i(z) - i_l(z)}{i_{fg}(z)} \tag{19}$$

The local specific enthalpy was found using the energy balance presented in Eq. (20), where i_{in} is the channel inlet enthalpy.

$$i(z) = i_{in} + \frac{q''_w (2H_{ch} + W_{ch}) z}{\dot{m}} \tag{20}$$

There is a temperature increase between the thermocouple location at the plenum inlet and the actual inlet to the microchannel. The fluid channel inlet temperature was thus calculated using Eq. (21). Note that operational parameters were adjusted at the time of experimentation to maintain a constant channel inlet subcooling of 10 K.

$$T_{in} = T_{inmeas} + \frac{q''_w A_{pl_{heat}}}{2\dot{m} c_{p_l}} \tag{21}$$

Two distinct regions in the channel were considered during two-phase flow experiments: namely, the single-phase and the two-phase region. In the single-phase region, the bulk fluid temperature was calculated from:

$$T_f(z) = T_{in} + \frac{q''_w (2H_{ch} + W_{ch}) z}{\dot{m} c_{p_l}} \tag{22}$$

The length of the subcooled region was calculated using:

$$L_{sub} = \frac{\dot{m} c_{p_l} (T_{sat\ z} - T_{in})}{q''_w (2H_{ch} + W_{ch})} \tag{23}$$

where $T_{sat\ z}$ is the saturation temperature at the location where the thermodynamic vapour quality is zero. This is dependent on the pressure at this location, which was calculated using Eq. (24). Therefore, an iterative procedure as outlined below was used to calculate the subcooled length due to its dependence on the local pressure which requires knowledge of the subcooled length.

$$P_{sat\,at\ L_{sub}\ (z)} = P_{in} - \frac{2 f_{sp} {G_{ch}}^2 L_{sub}}{\rho_l D_h} \tag{24}$$

The friction factor used in Eq. (24) was that proposed by Shah and London [42], which is presented in Eq (25). The fully developed Poiseuille number, $f_{FD}Re$, and the subcooled dimensionless length, L^*, were calculated using Eq. (26) and Eq. (27), respectively. α^* is a parameter similar to the channel aspect ratio α. However, in this case, it is the ratio of the shortest length to the largest length and always retains a value between 0 and 1. K_∞ and C are the dimensionless pressure drop number and dimensionless correction factor proposed by Shah and London, respectively. The values for K_∞ and C were obtained from a table provided by Shah and London and were found to be 1.43 and 0.00029, respectively.

$$f_{sp} = \frac{3.44}{Re\sqrt{L^*}} + \frac{f_{FD}Re + \frac{K_\infty}{4L^*} - \frac{3.44}{\sqrt{L^*}}}{Re\left(1 + \frac{C}{{L^*}^{-2}}\right)} \tag{25}$$

$$L^* = \frac{L_{sub}}{ReD_h} \tag{26}$$

$$f_{FD}Re = 24\left(1 - 1.355\alpha^* + 1.946{\alpha^*}^2 - 1.7012{\alpha^*}^3 + 0.9564{\alpha^*}^4 - 0.2537{\alpha^*}^5\right) \tag{27}$$

The saturated region length could then be found, after the iterative process to find the subcooled region length, using Eq. (28).

$$L_{tp} = L_{ch} - L_{sub} \tag{28}$$

The two-phase pressure drop could also be found after completion of the iterative process to find the subcooled length and the consequent pressure at that channel location, as shown in Eq. (29).

$$\Delta P_{tp} = \Delta P_{ch} - \frac{2 f_{sp} G_{ch}{}^2 L_{sub}}{\rho_l D_h} \tag{29}$$

The reliance on parameters between Eq. (11) and Eq. (29) meant that the data reduction was performed iteratively until a converged solution was found. Therefore, it is necessary to present the parameters on which the calculation of the heat transfer coefficient is dependent.

The local single-phase heat transfer coefficient in the subcooled region of the channel was calculated using:

$$h_{sp}(z) = \frac{q''_w}{T_w(z) - T_f(z)} \tag{30}$$

The single-phase Nusselt number for validation of the experimental facility could then be calculated from Eq. (31).

$$\overline{Nu} = \frac{D_h}{L_{ch} k_l} \int_0^{L_{ch}} h_{sp}(z) dz \tag{31}$$

The Reynolds number used for the single-phase validation of the experimental facility was calculated using:

$$Re = \frac{G D_h}{\mu_l} \tag{32}$$

The local two-phase heat transfer coefficient was calculated as:

$$h_{tp}(z) = \frac{q''_w}{T_w(z) - T_{sat}(z)} \tag{33}$$

Finally, the average two-phase heat transfer coefficient was calculated using Eq. (34).

$$\overline{h_{tp}} = \frac{1}{L_{tp}} \int_{L_{sub}}^{L_{ch}} h_{tp}(z)\, dz \tag{34}$$

All fluid thermophysical properties for HFE-7100 were obtained using the Engineering Equation Solver (EES) software. Prior to experimentation, the fluid was degassed by vigorously boiling the fluid in the test section for one hour before a vacuum pump was used to remove any trapped non-condensables from the reservoir. Full degassing was assessed through temperature and pressure measurements in the reservoir and their comparison to the saturation curves found in EES. Thermocouples and absolute pressure transducers were calibrated using an ASL F250 MK II precision reference thermometer (accuracy of 0.25 mK) and dead weight apparatus (accuracy ±0.01 %), respectively. The Krohne Optimass Coriolis flow meter was calibrated by the manufacturer (Krohne) at their facility and the differential pressure transducers were calibrated by Omega prior to shipping and installation in the experimental facility.

Uncertainties were calculated using the error propagation methodology outlined in Coleman and Steele [43] based on the generic equation given below:

$$U_r = \sqrt{\left\{\frac{\partial r}{\partial X_1} U_{X1}\right\}^2 + \left\{\frac{\partial r}{\partial X_2} U_{X2}\right\}^2 + \ldots + \left\{\frac{\partial r}{\partial X_j} U_{Xj}\right\}^2} \tag{35}$$

where X_1, X_2 and X_j are the measured parameters with the uncertainties of U_{X1}, U_{X2} and U_{Xj}.

The final uncertainty values of all measured and calculated parameters are presented in Table 2.

Table 2
Experimental uncertainties.

Experimental Parameter	Uncertainty
Inlet Temperature	± 0.011 - 0.039 K
Inlet Pressure	± 0.038 kPa
Differential Pressure	±0 0.080 - 0.168 %
Mass Flux	± 0.57 %
Local Vapour Quality	± 1.99 – 8.55 %
Heat Flux	± 2.39 - 4.10 %
Wall Superheat	± 0.034 – 0.089 K
Fanning Friction Factor	± 2.44 – 11.61 %
Average Nusselt Number	± 4.37 – 6.83 %
Local Heat Transfer Coefficient	± 3.97 – 7.17 %
Average Heat Transfer Coefficient	± 5.31– 9.82 %

3. Results and discussion

3.1. Single-phase validation and reproducibility

Single-phase experiments were conducted to validate the instrumentation and experimental methodology. Fig. 6 and Fig. 7 presented the experimental Fanning friction factor (f_{sp} from eq. 10) and mean single-phase Nusselt number (from Eq. 31) against Reynolds number (given by Eq. 32), respectively.

The single-phase friction factor was compared to the correlations provided by Shah and London [42] for both developing and developed laminar flows in rectangular ducts. Surprisingly, the data found better experimental agreement with the correlation for developing flows, but the experimental results were located between the two correlations. The hydrodynamic entry length for laminar flow in a rectangular duct can be approximated using Eq. (36) [44].

$$L_e \approx 0.05 \cdot Re \cdot D_h \tag{36}$$

It is estimated that 63 % of the channel was hydrodynamically developed for the lowest investigated Reynolds number (Re = 480) and 38 % was hydrodynamically developed for a Reynolds number of 1200. The hydrodynamically developing region occupies the entirety of the channel at a Reynolds number of 1920. It is therefore to be expected from the above, that the data becomes more aligned with the prediction for developing flows at higher Reynolds numbers due to the greater percentage of the channel being occupied by hydrodynamically developing flow.

The MAE % between the experimental data and the correlations for developing and developed flow was calculated using Eq. (37) and were 25.81 % and 8.36 %, respectively.

$$\text{MAE\%} = \frac{1}{n} \sum \left| \frac{X_{exp} - X_{pred}}{X_{exp}} \right| \times 100\% \tag{37}$$

The single-phase Nusselt number to Reynolds number is compared to the correlations provided by Jiang et al. [45] and Lee and Garimella [46] in Fig. 7. The experimental data were in good agreement with the correlations provided by Jiang et al. [45] and Lee and Garimella [46], producing MAE %s of 9.6 % and 9.27 %, respectively.

A repeatability experiment was conducted for a mass flux of 500 kg/m^{2}s at a system inlet pressure of 1 bar over 3 days. The boiling curves for the repeatability experiments are presented in Fig. 8. The repeatability of the experiment was very good with MAE %s between day 1 and 2, day 2 and day 3 and day 1 and day 3 being 7.36 %, 15.64 % and 6.82 %, respectively.

3.2. Heat transfer results

3.2.1. Flow visualisation

Flow visualisation presented four generic flow pattern categorisations of bubbly, slug, churn and annular flows. The four generic categorisations are presented in Fig. 9 for a mass flow rate of 400 kg/

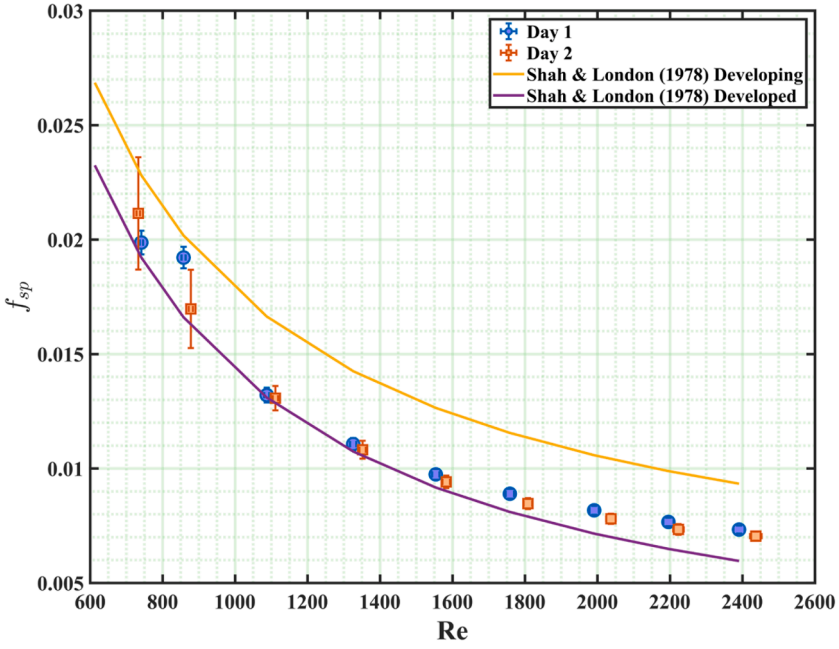

Fig. 6. Single-phase Fanning friction factor vs Reynolds number.

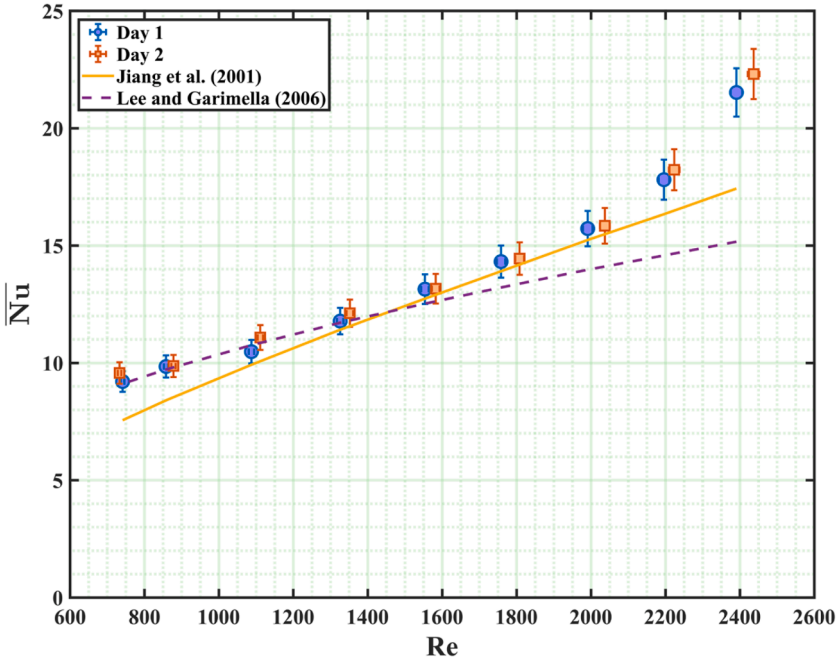

Fig. 7. Nusselt number vs Reynolds number.

m^2s. The camera was located near the channel outlet for this sequence of photographs taken at an increasing heat flux. Fig. 9 (a) presents bubbly flow in the saturated region. In this saturated region, vapour bubbles continued to grow, even when the bubbles did not appear to be in direct contact with the channel walls. This phenomenon may occur possibly due to the fact that the vapour bubble interface is in contact with a superheated liquid film at the channel wall. It can therefore be inferred that the superheated liquid film was able to evaporate into the vapour bubble as the bubble moved along the channel and the liquid film. There is no condensation when the bubbles enter the main stream liquid flow as this is at saturation conditions, resulting in overall bubble growth. The bubbles then coalesced with other bubbles to form large, confined bubbles that were categorised as the slug flow presented in Fig. 9 (b). However, bubbles were still able to nucleate in the film during slug flow. This phenomenon was attributed to the rectangular cross section of the channel, resulting in a larger liquid film at the corner of the channels. This is displayed diagrammatically in Fig. 10. Note that, even during slug flow, some localised dry spots were observed.

Eventually, the confined vapour bubbles of slug flow grew such that the interface became unstable and resulted in a chaotic mixture of phases. This resulted in the churn flow pattern shown in Fig. 9 (c). The resettlement of the phases resulted in a periodic, unsteady annular flow that is shown in Fig. 9 (d). During annular flow, a liquid film surrounded a vapour core. Periodically, the liquid film would begin to thin and cause

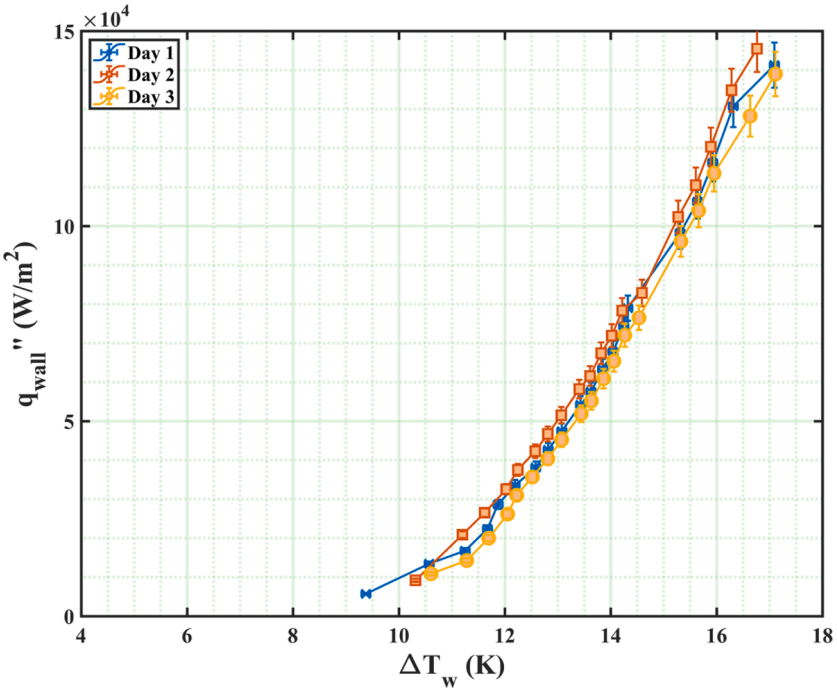

Fig. 8. Boiling curve for 500 kg/m^{2}s mass flux with an inlet pressure of 1 bar at z/L = 0.5, demonstrating reproducibility of the results.

local dry-out spots. The increased vapour quality at the exit of the channel resulted in plugging of the outlet plenum and the resultant compressibility effects increased the channel inlet pressure. Eventually, the pressure became relieved, and the upstream churn flow would rewet the channel walls into the initial annular flow configuration. Immediately after the rewetting of the walls, the liquid film thickness was sufficient that bubble nucleation in the corners of the channel was no longer suppressed and small micro bubbles were departing from the liquid film into the vapour core. As the liquid film thickness is reduced and dry out spots occurred, this bubble nucleation became suppressed once more. However, bubble nucleation was observed for all visualised flow patterns.

It is worth mentioning that the flow development is different in subcooled boiling conditions. In the subcooled region, bubbles began to grow (initially again from the corner of the channels) as long as they were in contact with the channel wall. However, once the bubble left the channel wall, the superheated microlayer at the wall was no longer able to evaporate and in the subcooled bulk fluid the vapour bubbles began to condense. This phenomenon is presented in the sequence of images shown in Fig. 11. As seen in the figure, bubble A remains attached to the wall and continues to grow between t=0 ms to the end of the sequence captured by the camera at t= 9.516 ms. However, bubble B, appearing at t=0.81 ms, leaves the wall and travels downstream in the main liquid flow, which is at a temperature below saturation. Condensation of the vapour of the bubble occurs and it shrinks in size, as seen in the subsequent timesteps to t=9.516 mm.

3.2.2. Heat transfer results

Local heat transfer rates and heat transfer coefficient were calculated at 9 locations along the channel. Fig. 12 depicts the boiling curves for channel inlet pressures of 1 bar, 1.5 bar and 2 bar at the centre location of the channel, i.e. z/L = 0.5. Temperature overshoot (TOS) was observed for all inlet pressures. However, the presence of TOS did not appear for all mass fluxes and its presence appeared randomly. The likely cause of the absence of TOS was the possible concentration of trapped vapour in the microcavities left from the previous experimental run. If large amounts of vapour were trapped in the microcavities, i.e. large embryos were present, the required wall superheat to activate bubble nucleation was lowered and the TOS was not observed. An example of this is observed in the boiling curve for 1000 kg/m^{2}s for a channel inlet pressure of 1.5 bar.

The results also showed that the wall superheat at the onset of boiling (ONB) was lower for higher system pressures. This phenomenon can be explained by considering the superheated boundary layer-based model presented by Hsu [47] for the required wall superheat for cavity activation during pool boiling. Superheated boundary layer-based models consider the thermal boundary layer at the heated wall and suggest that nucleation occurs when the temperature of the liquid in the boundary layer is equal to or greater than that of the vapour trapped inside the bubble. Hsu predicted the wall superheat required to activate a cavity containing trapped vapour using the superheated boundary layer-based incipience model, proposing the quadratic equation presented in Eq. (38) below.

$$r_c(\max,\min) = \frac{\delta_{th}}{2}\cdot\frac{\sin\varphi\Delta T_{sup}}{(1+\cos\varphi)(\Delta T_{sup}+\Delta T_{sub})}\left[1\pm\sqrt{1-\frac{8(1+\cos\varphi)\sigma T_{sat}(T_{sup}+T_{sub})}{\delta_{th}\rho_v i_{fg}\Delta T_{sup}{}^2}}\right] \tag{38}$$

In Eq. (38), $r_c(max,min)$ represents the maximum and minimum cavity mouth radii in which a cavity with a trapped vapour embryo will become active. Hence, any cavities with a cavity mouth radius between these two values will become active for a given wall superheat. The resultant relationship between cavity mouth radius and the required

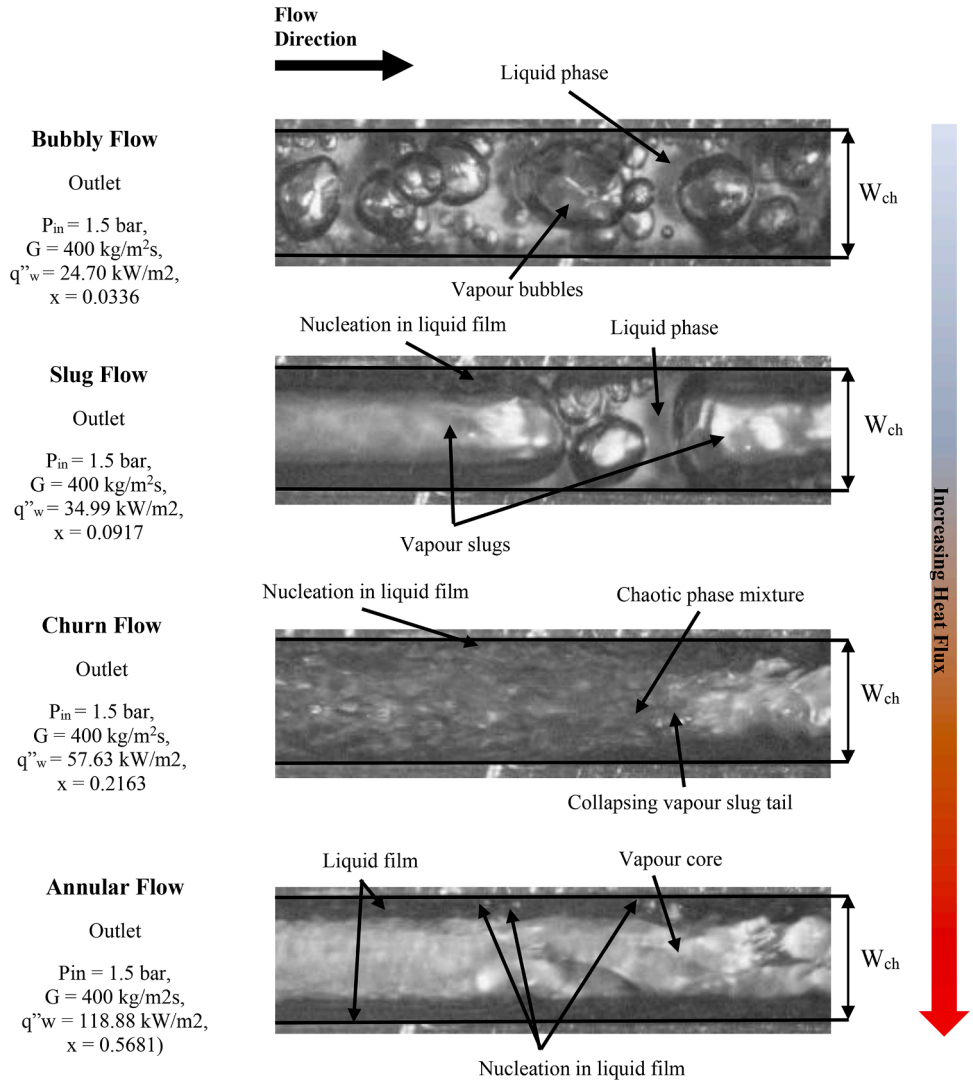

Fig. 9. Observed flow patterns in the saturated region with generic classifications.

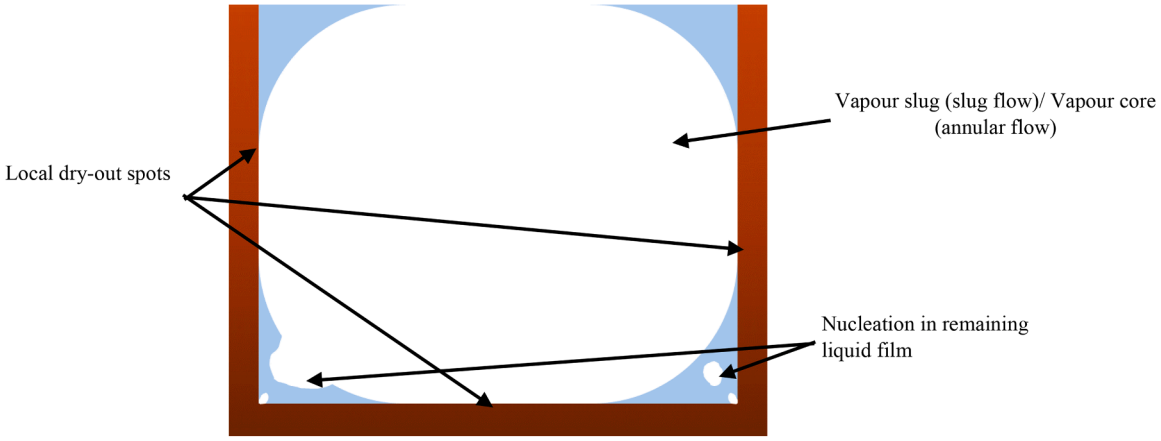

Fig. 10. Cross section of channel with simultaneous dry spots and bubble nucleation.

wall superheat is presented in Fig. 13 for HFE-7100 at 1 bar, 1.5 bar and 2 bar. In Eq. (38), φ represents the contact angle between the bubble embryo and the boiling surface. Hsu estimated that the contact angle was equal to 53.1° based on the assumption that the liquid temperature is equal to the temperature at the top of the bubble. The thermal boundary layer thickness, δ_{th}, was estimated as the ratio of the liquid phase thermal conductivity to the single-phase heat transfer coefficient (mean value of h_{sp} calculated by Eq. 30). Finally, a subcooling of 5 K (average of the inlet degree of subcooling of 10 K and saturated conditions) was assumed to calculate liquid-phase thermophysical properties,

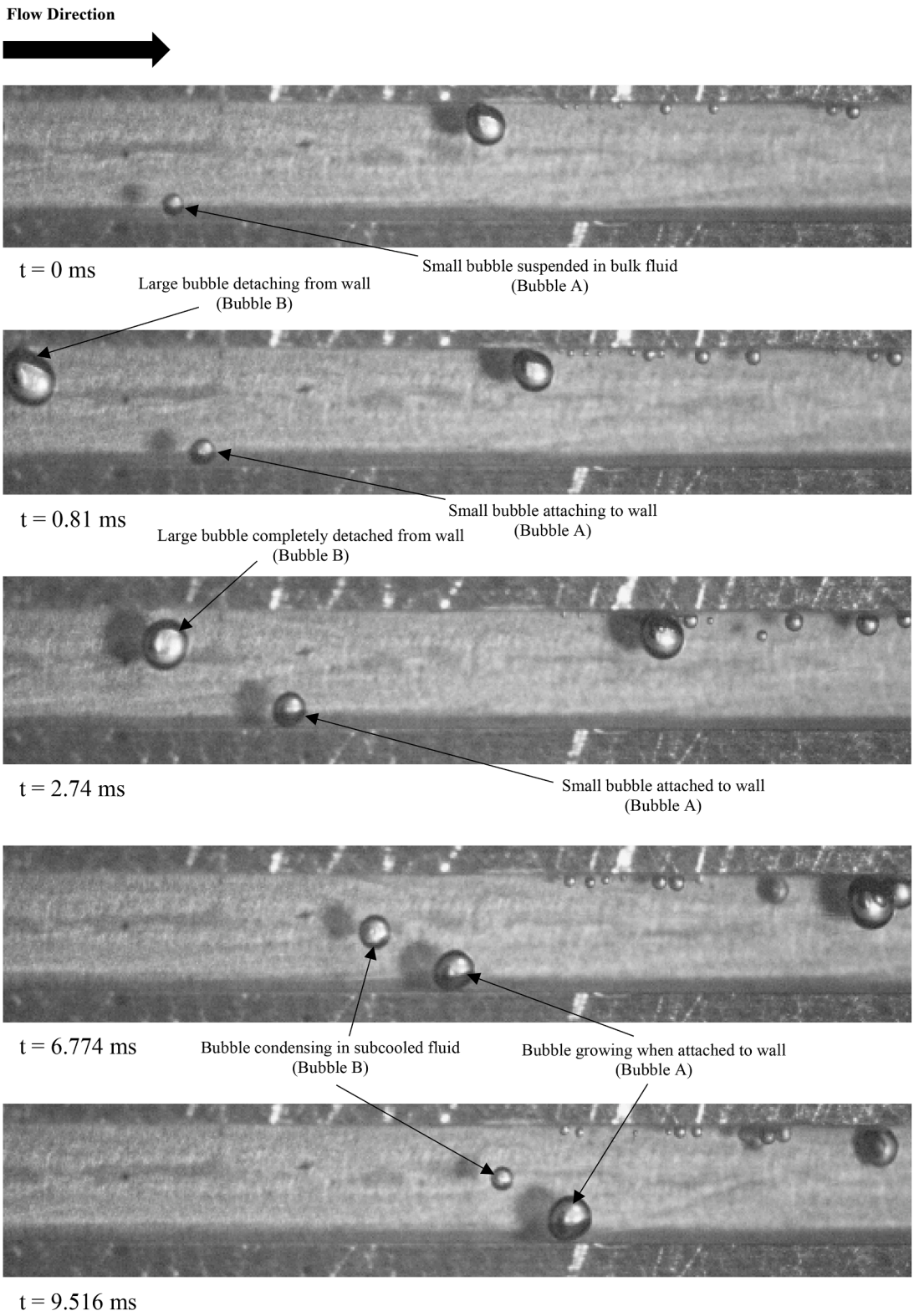

Fig. 11. Bubble nucleation and departure at the channel outlet in the subcooled region (Pin = 1.5 bar, G = 500 kg/m^{2}s, q"$_w$ = 19.79 kW/m^2, x_{out} = -0.0072).

whilst the vapour-phase thermophysical properties were calculated at saturation conditions.

The figure shows that, whilst the cavities with larger mouth radii are unaffected, smaller microcavities become active at lower wall superheats as the system pressure increases. Therefore, the Hsu model predicts that more cavities are activated at lower wall superheats for HFE-7100 at higher system pressures. This helps to explain two phenomena presented in Fig. 12. The first is that the ONB occurs at lower wall superheats for higher system pressures, which is potentially a result of smaller cavities that would not be active at lower system pressures, become active. The second is the lower wall superheats, i.e. higher heat transfer coefficients, that occur at higher system pressures. This is likely a result of a greater range of cavity radii becoming active, increasing the bubble nucleation site density.

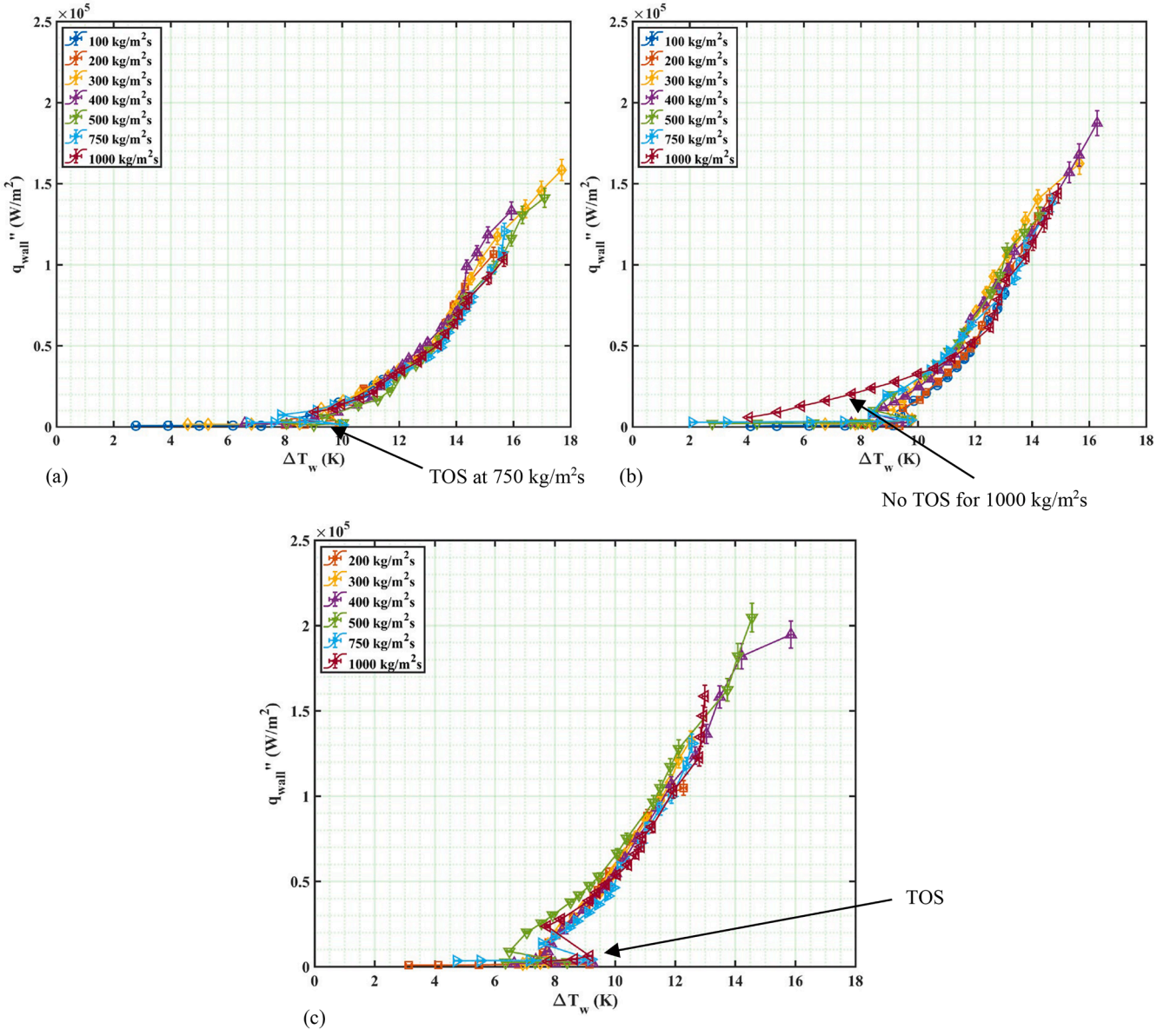

Fig. 12. Boiling curves at z/L = 0.5: (a) for 1 bar; (b) for 1.5 bar; (c) for 2 bar.

Fig 12. also indicates that there is no clear effect of mass flux on the boiling curve. This finding was not unique to this study and was also observed by other researchers [17,48–50]. The local heat transfer coefficients are plotted against vapour quality in Fig. 14 for a mass flux of 400 kg/m^{2}s at the three channel inlet pressures. The heat transfer coefficients were found to decrease with local vapour quality but increase significantly with wall heat flux. This can be linked back to the flow patterns observed in Fig. 9, with the transition boundaries included in Fig. 14. As the flow patterns progress out of the bubbly flow regime the presence of dry spots begins to occur. These dry spots decrease the local heat transfer coefficient. However, the increased heat flux (increasing wall superheat) results in more active nucleation sites in the liquid film that may explain the strong heat flux effect, which persists in slug, churn and annular flow.

Furthermore, the liquid film evaporation during slug and annular flows may also be aided by the increased heat flux. Fig. 15 presents the effect of mass flux on the local heat transfer coefficients with respect to the non-dimensional length, which once again show no clear mass flux effect in the two-phase region. It is also clear from the figures, that an increasing mass flux will result in a larger portion of the test section being in single-phase with a subsequent effect on the local heat transfer coefficient, i.e. lower value of the heat transfer coefficient compared to values at lower mass flux where boiling was established.

Although a minimal effect of mass flux on heat transfer was observed, the mass flux did have a small effect on wall temperature, particularly at lower system pressures. This effect can be seen in Fig. 16, which plots both the local fluid temperature and local wall temperatures. The two-phase pressure drop was found to decrease with an increase in channel inlet pressure and increase with mass flux. This meant that the local fluid temperature decreased more dramatically along the channel with higher mass fluxes. Therefore, the channel wall temperature was lower despite the local heat transfer coefficient being largely unaffected in the two-phase region. This affect was found to be lowered with an increase in channel inlet pressure due to the lower two-phase pressure drop.

3.3. Comparison to existing correlations

Table 3 includes the heat transfer correlations selected in this study for comparison with the new experimental data. The correlations were

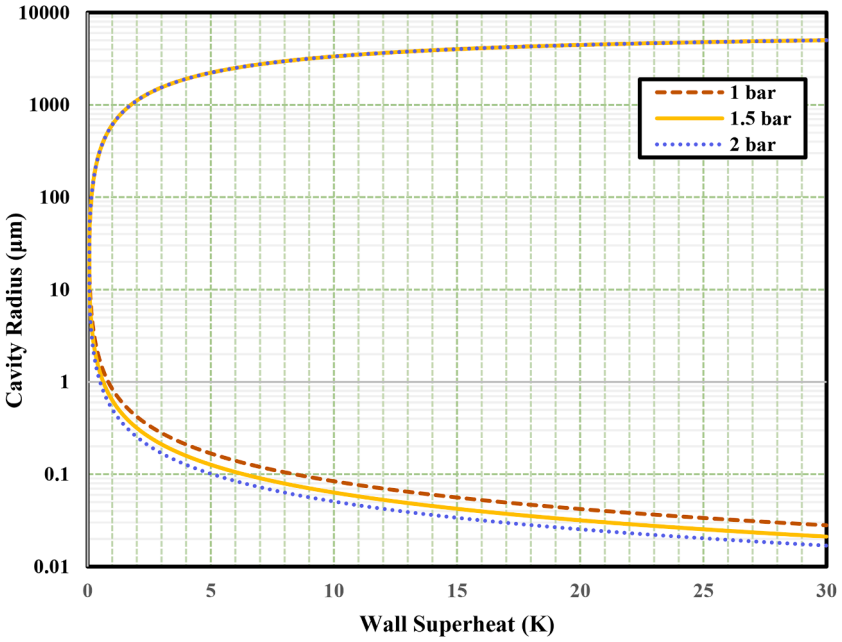

Fig. 13. Effective nucleation cavity radii with respect to wall superheat according to Hsu [47].

selected based on existing comparisons by Al-Zaidi et al. [17] and [25] and Lee [51], as these correlations performed well in their analyses or are new and have not yet been investigated in these studies. Correlations that performed particularly poorly in their studies were omitted, as their findings have already indicated that these correlations are not generally reliable, even if they might perform well in their specific context.

A comparison of the new experimental data to the eight existing heat transfer correlations shown in Table 3 is displayed in Fig. 17. The compared correlations were developed for using data for conventional size channels, multi-microchannel heat sinks and vertical mini-tubes. Eq. (37) was used to determine the MAE % for each of the correlations and the percentage of data points within the ±30 % error region (θ_{30}) was also calculated.

A correction factor was applied to some of the correlations that were proposed for fully heated channels, i.e. in which all sides of the channel were heated. The new experimental data were obtained for a single microchannel in which the top plate was not considered to be heated and thus, the correction factor presented in Eq. (39) was applied, as previously adopted in other studies [17,52,53]:

$$h_{tp,\ mod} = \left(\frac{Nu_3}{Nu_4}\right) h_{tp} \tag{39}$$

where $h_{tp,\ mod}$, is the modified two-phase heat transfer coefficient, Nu_3, Nu_4 the thermally developed and developing single-phase laminar flow Nusselt number for a channel with three and with four heated sides respectively and h_{tp} the predicted two-phase heat transfer coefficient.

The Nusselt number for thermally developed flow in a channel with three heated sides and the Nusselt number for thermally developed flow in a channel with four heated sides are shown in Eq. (40) and Eq. (41), respectively, as proposed by Shah and London [42].

$$Nu_3 = 8.235\left(1 - 1.833\alpha^* + 3.767\alpha^{*2} - 5.814\alpha^{*3} + 5.361\alpha^{*4} - 2\alpha^{*5}\right) \tag{40}$$

$$Nu_4 = 8.235\left(1 - 2.042\alpha^* + 3.085\alpha^{*2} - 2.477\alpha^{*3} + 1.058\alpha^{*4} - 0.186\alpha^{*5}\right) \tag{41}$$

As seen in Table 3, Shah [54] proposed a flow boiling heat transfer correlation for conventional tubes that selects the greater heat transfer coefficient between nucleate and convective boiling. They related the nucleate boiling component (E) to the Boiling number and the convective component (S) to the Convection number. This correlation was tested with experimental data for several fluids, such as water, R-11, R-12, R-22, and R-113, in both vertical and horizontal channels with diameters ranging from 6 to 25.4 mm. This correlation was only able to predict 35.2 % of the current experimental data points within 30 % of the predicted value and provided an overall MAE % of 58.47 %. The poor prediction of the current experimental data is to be expected as the correlation was developed using data for conventional sized tubes and could not capture any microscale effects.

Warrier et al. [55] carried out an experimental investigation on flow boiling of FC-84 in horizontal rectangular multi-microchannels. The aluminium heat sink featured five parallel channels with a hydraulic diameter of 0.75 mm. Their experiments covered heat fluxes up to 59.9 kW/m^2 and mass fluxes ranging from 557 to 1600 kg/m^{2}s. The proposed correlation, included in Table 3, incorporated the Boiling number and vapour quality, along with a single-phase heat transfer coefficient for fully developed laminar flow. It was valid for the ranges $0.03 \leq x \leq 0.55$ and $0.00027 \leq Bo \leq 0.00089$. The Bo number of the present experiments was 0.0000136 to 0.0071. Consequently, only 55.14 % of data points were within the valid correlation range. This correlation [51] performed poorly in predicting the present experimental data, with only 38 % of the points falling within 30 % of the predicted value and yielding a MAE % of 48.20 %. This limited predictive accuracy can be attributed to the narrow development conditions under which the correlation was derived, specifically a single working fluid (FC-84), single-channel geometry and limited boiling number range, which limit its applicability to broader microscale flow boiling scenarios.

Lee and Mudawar [21] conducted experiments on flow boiling heat transfer using water and R134a in horizontal parallel rectangular microchannels. The microchannels, made of oxygen-free copper, had a hydraulic diameter of 0.348 mm. The experiments were carried out at heat fluxes between 159 and 938 kW/m^2 and mass fluxes from 127 to 654 kg/m^{2}s. As seen in Table 3, they developed three correlations for different vapour quality ranges: $x \langle 0.05$, $0.05 < x < 0.55$, and $x \rangle 0.55$. Their results showed that nucleate boiling dominated at vapour qualities below 0.05, while convective boiling was more significant at moderate and high qualities. The heat transfer coefficient was expressed as a function of the liquid Weber number, Boiling number, Martinelli parameter, and single-phase heat transfer coefficient. The correlation

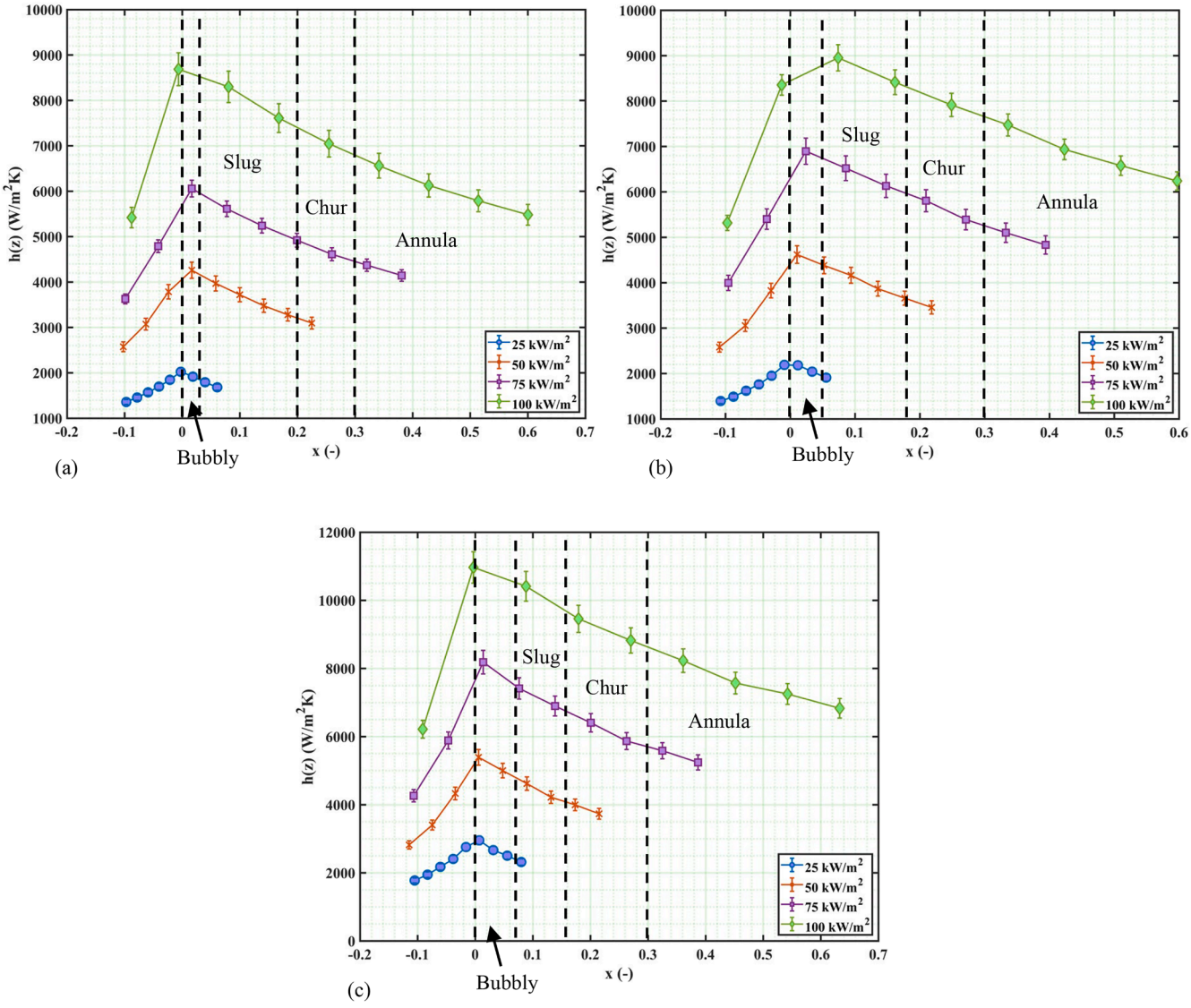

Fig. 14. Effect of heat flux on local heat transfer coefficient for a mass flux of 400 kg/m2s: (a) at 1 bar; (b) at 1.5 bar; (c) at 2 bar.

developed by Lee and Mudawar [21] was not well-suited to predict the present experimental data, yielding a MAE % of 77.24 % and accurately capturing only 18 % of the data points within 30 % of the predicted values. This poor performance can likely be attributed to the correlation's segmentation of flow boiling heat transfer mechanisms, specifically its distinction between nucleate and convective boiling regions across different vapour quality ranges ($x < 0.05$, $0.05 < x < 0.55$, and $x > 0.55$). In contrast, the current data exhibit characteristics that demonstrate nucleate boiling effects across all vapour qualities. The discrepancy between the experimentally observed presence of nucleate boiling contribution in all flow regimes and the correlation's segmented approach appears to hinder its accuracy, as the correlation assumes a shift to convective boiling at moderate and high vapour qualities. As a result, the predictive power of this correlation is limited in scenarios where nucleate boiling persists to a certain degree throughout the entire range of vapour qualities, as is the case with the current study.

Mahmoud and Karayiannis [56] examined the flow boiling heat transfer of R134a in vertical tubes with diameters ranging from 0.52 to 4.26 mm. They developed an empirical correlation that included an enhancement factor (F) based on an approach proposed by Chen [57]. Their correlation, given in Table 3, also utilised Cooper's [58] pool boiling correlation (h_{coop}) to consider the effect of nucleate boiling. The correlation developed by Mahmoud and Karayiannis [56] demonstrates strong predictive accuracy with a MAE % of 16.8 % and captures 87.6 % of the data points within 30 % of the measured values, performing well despite being developed for vertical tubes. This success can likely be attributed to the correlation's ability to capture the nucleate boiling contribution through the Cooper [58] pool boiling component, Sh_{coop}, which aligns well with the characteristics observed in the current experimental data. As illustrated in Fig. 18, Sh_{coop} frequently dominates the total heat transfer coefficient, underscoring the significance of nucleate boiling across various flow conditions. This effective handling of nucleate boiling enables the correlation to adapt well, even under conditions that differ from its original development parameters. Experimental results for multi-channels provided by Al-Zaidi et al. [17], Fayyadh et al. [49] and Criscuolo et al. [59] and experimental results for vertical minichannels by Anwar et al. [60] and Asim et al. [61] also agreed well with this correlation for a wide range of refrigerants.

Lin and Jia [62] conducted an experimental investigation into the flow boiling heat transfer of R134a in horizontal rectangular multi-microchannels with a hydraulic diameter of 0.5 mm, heated on three sides. They categorized their findings into three regimes: Regime I corresponded to nucleate boiling, where the heat transfer coefficient increases with increasing heat flux for all mass fluxes, although the

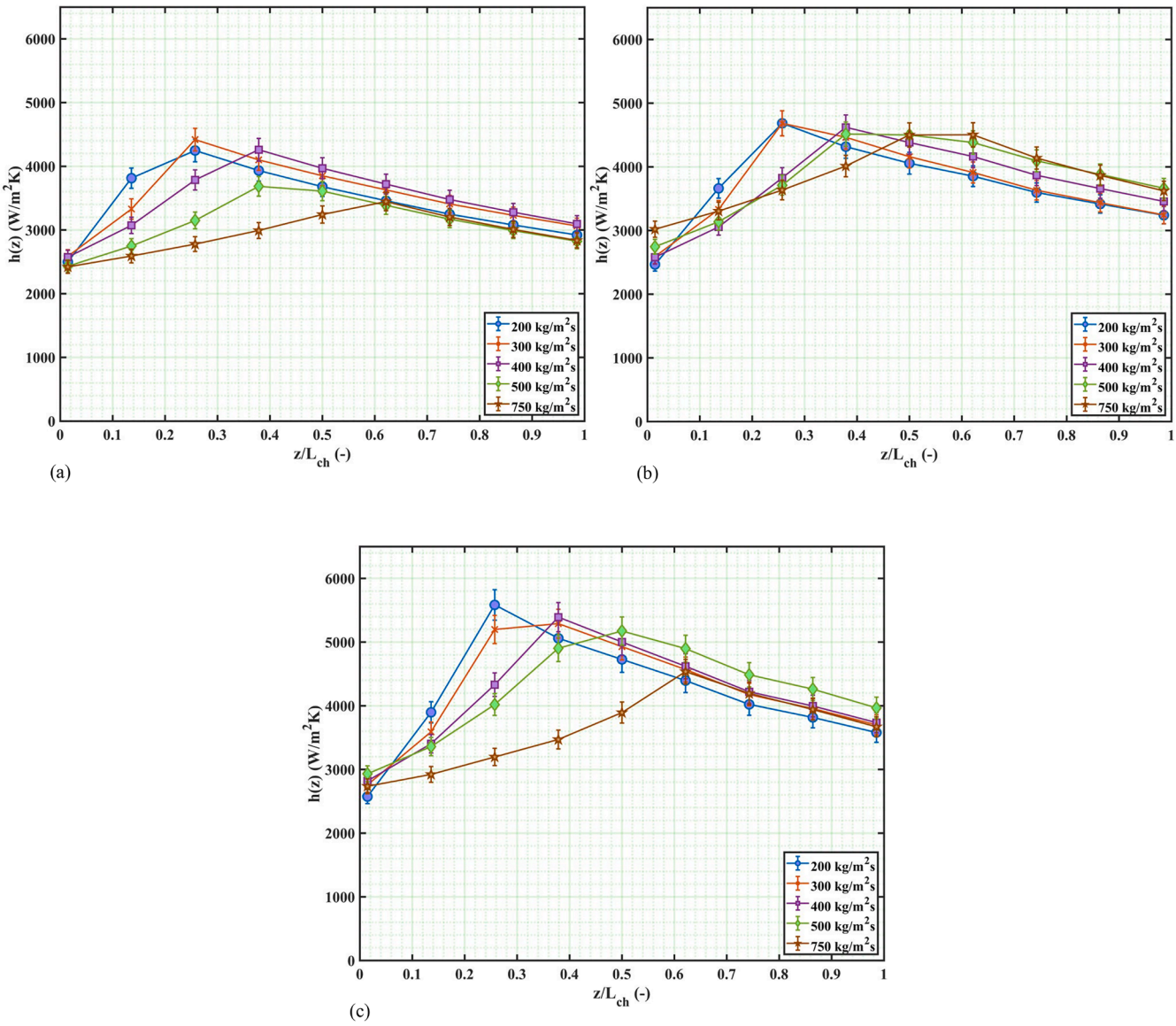

Fig. 15. Effect of mass flux on local heat transfer coefficient for a heat flux of 50 kW/m: (a) at 1 bar; (b) at 1.5 bar; (c) at 2 bar.

influence of mass flux was minimal. They also noted a slight decline in the heat transfer coefficient at higher heat flux levels. Regime II was characterized by convective boiling, where mass flux had a notable impact on the heat transfer coefficient, along with effects from heat flux itself. Regime III, known as the dry-out regime, was defined by a reduction in the heat transfer coefficient with increasing heat flux for most mass fluxes. Based on their observations, the authors developed two correlations to describe the nucleate boiling and convective boiling dominant regimes given in Table 3. The correlations developed by Lin and Jia [62] were not adequately suited to predict the experimental data from the current study, resulting in a MAE % of 1529.29 % and capturing only 13.6 % of the data points within 30 % of the predicted values. This substantial discrepancy is likely due to the correlation's reliance on distinct flow boiling regimes, including both nucleate and convective boiling, which may not align with the presence of nucleate boiling observed in the current experiments in all flow regimes. While their correlation attempts to account for varying influences of heat flux and mass flux across different regimes, the clear presence of nucleation sites across all flow regimes seen in our flow visualization and in the experimental data suggests that the correlation fails to accurately represent the heat transfer characteristics throughout the entire range of operating conditions. Consequently, the limited predictive capability of this correlation highlights the challenges associated with applying segmented approaches to scenarios where nucleate boiling has a sustained presence.

Thiangtham et al. [63] investigated flow boiling of R134a in horizontal multi-microchannels. They fabricated rectangular microchannels with a hydraulic diameter of 0.421 mm. Their results showed that at lower heat fluxes, the heat transfer coefficient increased with heat flux, indicating the prevalence of nucleate boiling. However, at elevated heat fluxes, the heat transfer coefficient was found to increase with mass flux, suggesting that convective boiling took over. From their data analysis, the authors developed a flow boiling heat transfer correlation based on dimensionless groups, seen in Table 3. This correlation [63]was not well-suited for the experimental conditions observed in this study, yielding a MAE % of 181.53 and failing to capture any data points within 30 % of the predicted values. This lack of predictive accuracy likely stems from the correlation's development based on a limited set of operating scenarios, which may not encompass the full range of conditions encountered in the current experiments. Although the authors identified distinct trends in heat transfer behaviour at varying heat fluxes and mass fluxes, the specific conditions under which their

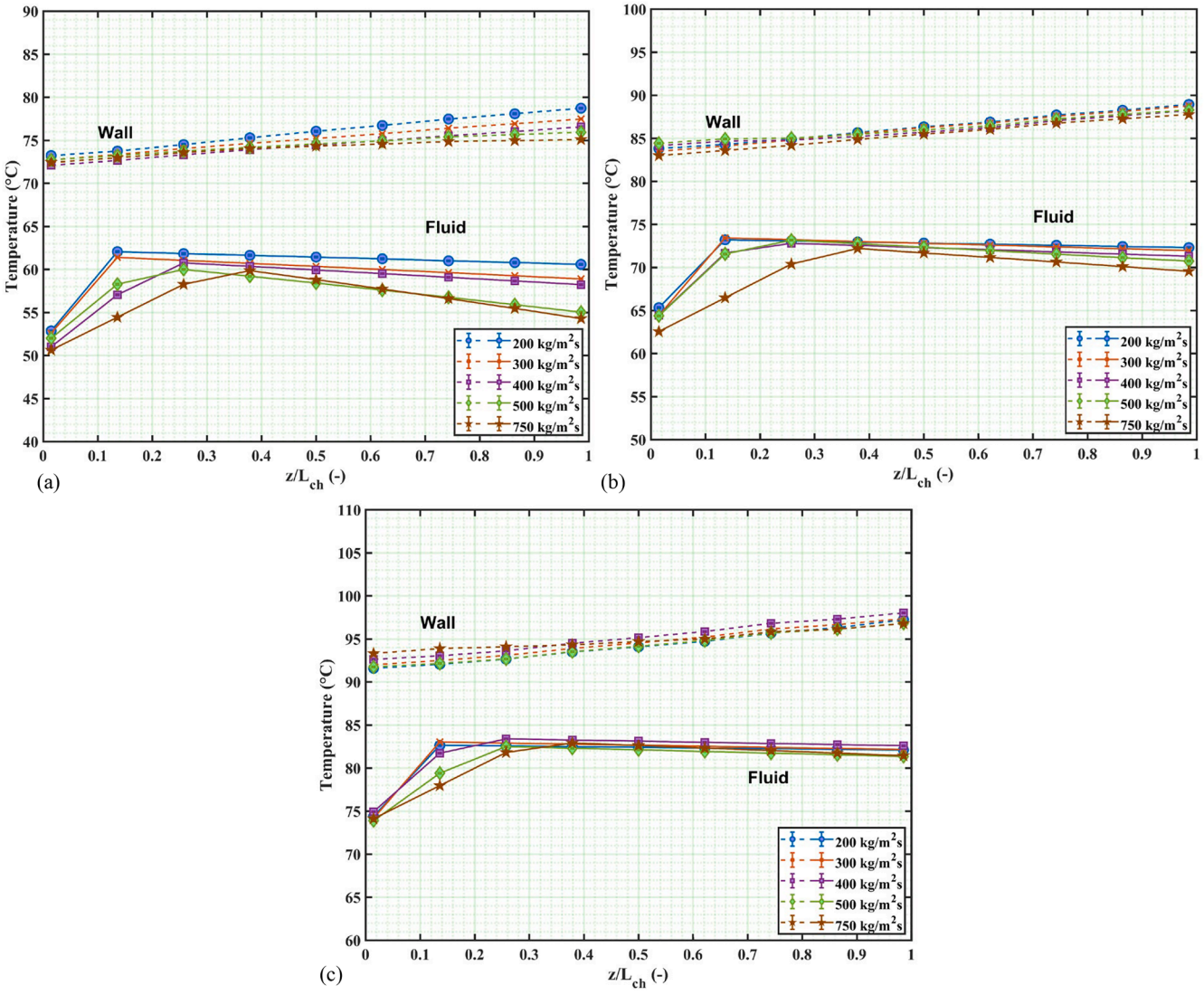

Fig. 16. Effect of mass flux on local wall and fluid temperatures for a heat flux of 100 kW/m: (a) at 1 bar; (b) at 1.5 bar; (c) at 2 bar.

correlation was formulated limit its applicability to scenarios of persisting nucleate boiling presence.

In 2017, Shah [64] assessed a comprehensive dataset in comparison to their earlier correlation from 1982. It was observed that this correlation accurately predicted most of the data; however, some underprediction occurred at low mass fluxes, which was linked to the influence of surface tension in those cases. To address this issue, the original correlation was improved by introducing a new correction factor (F) that incorporated the effects of the Weber number and Boiling number. The updated correlation, included in Table 3, was validated with an extensive dataset, which included thirty-one different fluids, analysed both vertical and horizontal flow conditions, and accounted for various channel geometries, as well as fully and partially heated channels with diameters ranging from 0.38 to 27.1 mm. The correlation developed by Shah [64] exhibited significant shortcomings in its predictive capability for the present experimental data, resulting in a MAE % of 244.32 % and capturing only 35.2 % of the data points within 30 % of the predicted values. While Shah attributed discrepancies in heat transfer predictions at low mass fluxes to confinement effects related to surface tension, this explanation may overlook the complex role that confinement can play in influencing dominant heat transfer mechanisms in microchannels. Given that this updated correlation is essentially a modification of the earlier 1982 correlation, it may be misapplying a convective boiling framework when the conditions observed in the current study suggest a need for the inclusion of a nucleate boiling model. Consequently, the limited scope of the modification could hinder the correlation's effectiveness in accurately predicting heat transfer behaviour across a broader range of flow conditions and geometries.

Zhang et al. [23] conducted a visualization-based experimental study to investigate the influence of hydraulic diameter on microchannel flow boiling heat transfer characteristics. Their experiments utilized deionized water as the working fluid, with microchannel diameters ranging from 250 μm to 1500 μm. The study employed three parallel microchannels, with heat fluxes varying between 203 and 880 kW/m^2, an outlet pressure of 101.325 kPa, and pressure drops ranging from 0.71099 to 18.021 kPa. The observed vapour quality spanned from 0.00183 to 0.37536. Due to discrepancies between existing predictive methods and their experimental data, the authors developed a new empirical correlation incorporating the liquid-only Reynolds number, Boiling number, and liquid-only Weber number to improve prediction accuracy. The correlation proposed by Zhang et al. [23] demonstrated limited predictive accuracy for the present dataset, yielding a MAE of 51.5 % and capturing only 40 % of the data within ±30 % of the predicted values. This discrepancy is likely due to the fact that their correlation was developed specifically for deionized water. While Zhang et al. accounted for a wide range of hydraulic diameters, their

Table 3
Existing flow boiling heat transfer correlations.

Author(s)	Correlation	Range of Applicability
Shah (1982)	$h_{tp} = Max(E,S)h_{sp}$ $S = 1.8/N^{0.8}$ *For* $1 < N$: $E = 230Bo^{0.5}\ (for\ Bo > 3 \times 10^{-5})$ $E = 1 + 46Bo^{0.5}\ (for\ Bo < 3 \times 10^{-5})$ *For* $0.1 < N \leq 1$: $E = FBo^{0.5}e^{2.74N^{-0.1}}$ *For* $N > 1$: $E = FBo^{0.5}e^{2.47N^{-0.15}}$ $F = 14.7\ (for\ Bo \geq 11 \times 10^{-4})$ $F = 15.43\ (for\ Bo < 11 \times 10^{-4})$ $N = N_{CO}\ (for\ Fr_{lo} \geq 0.04)$ $N = 0.38Fr_{lo}^{-0.3}N_{CO}\ (for\ Fr_{lo} < 0.04)$	D = 6–25.4 mm Fluids (water, R11, R12, R22, R113, cyclohexane) For saturated boiling in vertical and horizontal channels
Warrier et al. (2002)	$h_{tp} = \left[1 + 6Bo^{\frac{1}{16}} - 5.3(1 - 855Bo)x^{0.65}\right]h_{sp}$	D_h = 0.75 mm Fluid (FC-84) G = 557—1600 kg/m^{2}s q" = up to 59.9 kW/m^2 For saturated boiling in horizontal rectangular multi-channels
Lee and Mudawar (2005)	$h_{tp} = 3.856\chi^{0.267}h_{sp}\ (for\ 0 < x < 0.05)$ $h_{tp} = 436.48Bo^{0.522}We_{lo}^{0.351}\chi^{0.665}h_{sp}\ (for\ 0.05 < x < 0.55)$ $h_{tp} = Max\left\{(108.6\chi^{1.665}h_{sp,g})h_{sp,g}\right\},\ (for\ 0.55 < x < 1)$ $h_{sp,g} = \frac{Nu_3k_g}{D_h}\ (for\ laminar\ vapour\ flow)$ $h_{sp,g} = 0.023Re_{gs}^{0.8}Pr_g^{0.4}\frac{k_g}{D_h}\ (for\ turbulent\ vapour\ flow)$	D_h = 0.348 mm Fluids (water, R134a) G = 127−654 kg/m^2 s q" = 159−938 kW/m^2 For saturated boiling in horizontal rectangular multi-channels
Mahmoud and Karayiannis (2013)	$h_{tp} = Sh_{coop} + Fh_{sp}$ $h_{coop} = 55P_R^{0.12-0.2log_{10}Rp}\left(-log_{10}(P_R)\right)^{-0.55}M^{-0.5}q''_w{}^{0.67}$ $S = \frac{1}{1 + 2.56 \times 10^{-6}\left(Re_{ls}F^{1.25}\right)^{1.17}}$ $F = \left(1 + \frac{A}{\chi}\right)^{0.64}$ $A = 2.812C_o^{-0.408}$	D =0.52−4.26 mm Fluid (R134a) G = 100−700 kg/m^2 s q" = 1.7—158 kW/m^2 For saturated boiling in vertical single tubes.
Lin and Jia (2015)	For nucleate boiling regime: $h_{tp} = 189Bo^{0.178}Bd^{0.4}Re_{ls}^{0.12}\frac{k_l}{D_h}$ For convective boiling regime: $h_{tp} = 277.3Bo^{0.978}Re_{ls}^{0.94}(1-x)^{0.47}\frac{k_l}{D_h}$	D_h = 0.5 mm Fluid (R134a) G = 373.33−1244.44 kg/m2 s q" = up to 802.12 kW/m^2 For saturated boiling in horizontal rectangular multi-channels
Thiangtham et al. (2016)	$h_{tp} = \frac{10^{16.7}Bo^{0.3}We_{lo}^{2.7}k_l}{Re_{lo}^{4.95}\left(\frac{\rho_l}{\rho_g}\right)^{0.9}D_h}$	Dh = 0.421 mm Fluid (R134a) G = 150−600 kg/m2 s q" = 3—127 kW/m2 Tsat =13,18, 23 °C For saturated boiling in horizontal rectangular multi-channels
Shah (2017)	$h_{tp} = Fh_{Shah(1982)}$ $F = 2.1 - 0.008We_{go} - 110B$ *If* $F < 1$, *Use* $F = 1$	D = 0.38−27.1 mm Fluids (Water, CO2, R11, R12, R22, R32, R113, R123, R114, R123, R134a, R152a, R1234yf, R236fa, R245fa, ammonia, propane, isobutane, carbon tetrachloride, isopropyl alcohol, ethanol, methanol, n butanol, cyclohexane, benzene, heptane, pentane, argon, hydrogen, nitrogen, helium) G = 15−2437 kg/m2s For saturated boiling in vertical and horizontal (single and multi) channels
Zhang et al. (2025)	$h_{tp} = \frac{0.00344Re_{lo}^{1.23629}e^{0.6715x_{out}}}{Bo^{0.32148}We_{lo}^{0.467}}\frac{k_l}{D_h}$	Dh = 0.25 – 1.5 mm Fluid (water) $Re_l < 0$ $x < 0.4$ For saturated boiling in horizontal rectangular multi-channels

correlation may not fully capture the thermophysical differences between water and refrigerants, particularly in terms of surface tension, latent heat, and viscosity effects. These differences could significantly impact the dominant heat transfer mechanisms, leading to the observed deviations in predictive performance. Furthermore, the correlation is only applicable for exit vapour qualities less than 0.4, whereas the data in this study far exceeds this.

Significant discrepancies exist between the performance of the different proposed predictive tools, highlighting the complexity and variability inherent in flow boiling heat transfer. However, among the various correlations evaluated, the empirical correlation developed by Mahmoud and Karayiannis [56] emerged as the most accurate correlation for heat transfer rates in flow boiling scenarios, consistently demonstrating superior predictive capability. The current research underscores the necessity for further research to refine and enhance these predictive models, ensuring their reliability across a broader range of operating conditions. Nevertheless, based on current evaluations, the correlation by Mahmoud and Karayiannis is recommended for its robust performance in capturing the dominant heat transfer mechanisms observed in the present study and their effect on the heat transfer

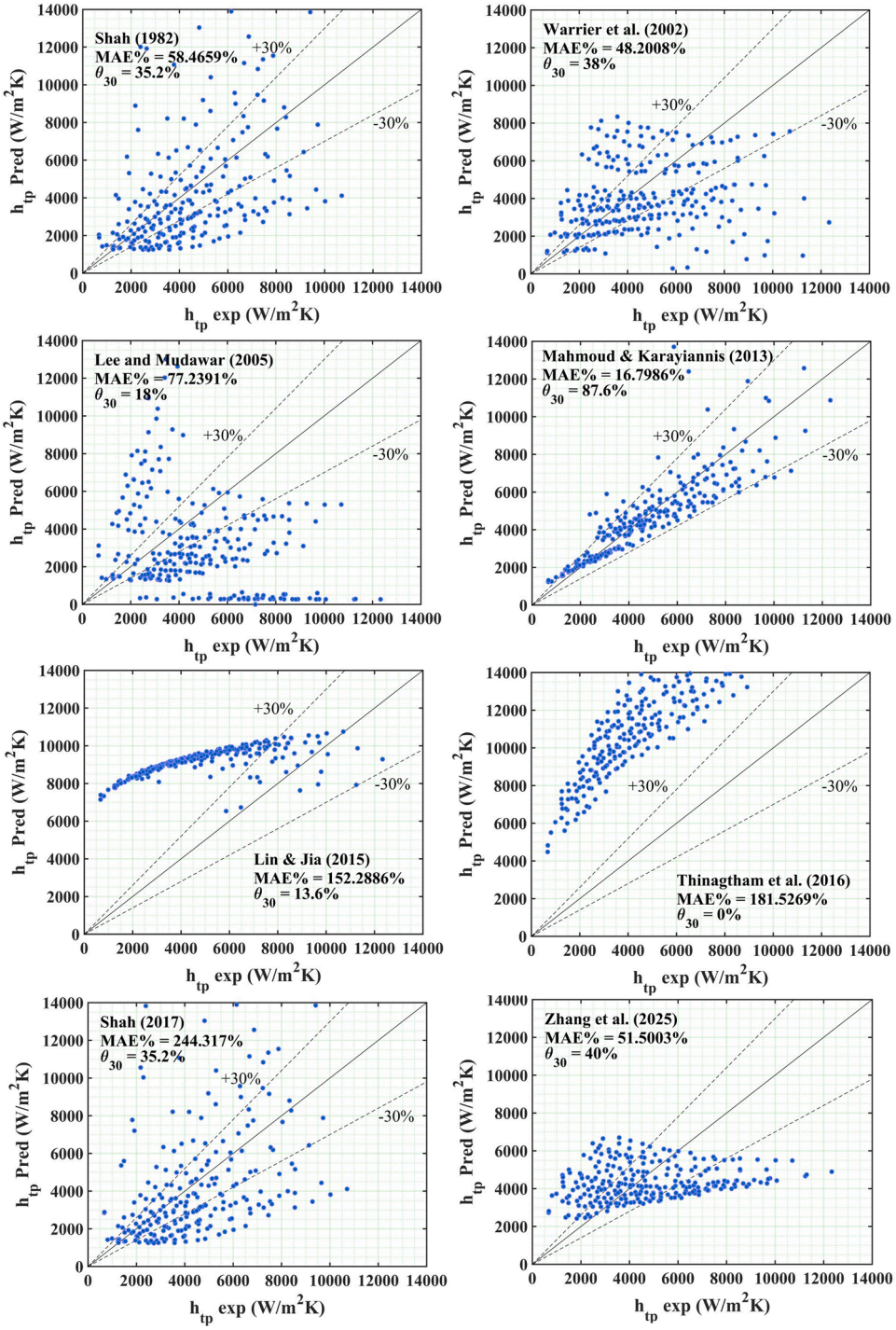

Fig. 17. Comparison of new heat transfer results to existing correlations.

coefficient.

4. Conclusions

HFE-7100 was used in this study to investigate flow boiling in a single microchannel. In this study, four primary flow patterns—bubble, slug, churn, and annular—were observed in the microscale flow boiling process, each with unique characteristics tied to the flow dynamics under microscale conditions. These distinct patterns help illustrate the complex interaction between the liquid and vapour phases in confined microscale channels, a critical factor for accurate modelling and prediction in microscale heat transfer applications.

The study calculated local heat transfer coefficients at nine locations along the channel, revealing that temperature overshoot was observed for all inlet pressures but appeared randomly across different mass fluxes. The absence of TOS was likely due to trapped vapour in microcavities from previous experiments. Results indicated that higher system pressures lowered the wall superheat required for the ONB, activating more cavities at lower superheats for the investigated fluid and test section surface morphology.

No clear effect of mass flux on the boiling curve was observed in the saturated region of the channel. The heat transfer coefficient increased with wall heat flux and decreased with local vapour quality in the saturated region. This was explained by the constant bubble nucleation

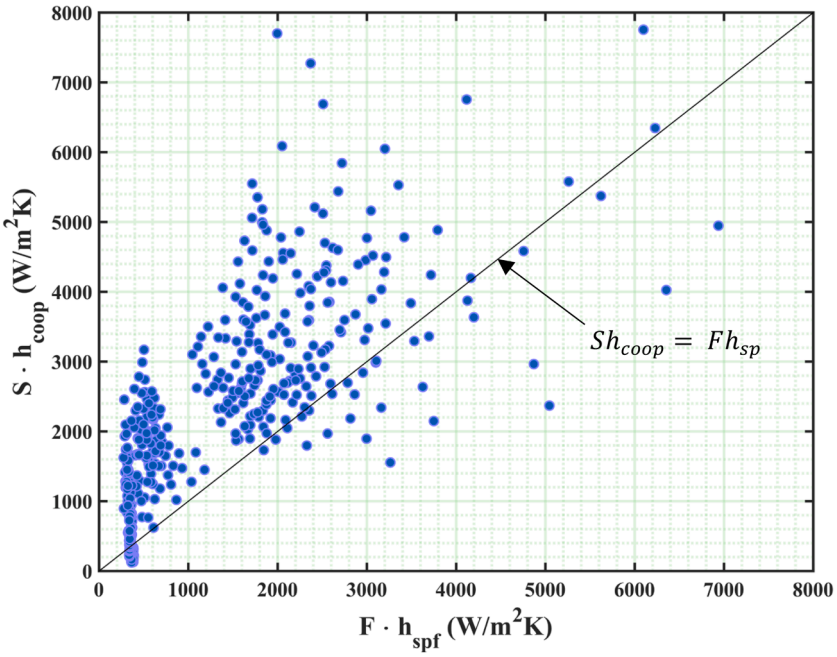

Fig. 18. Comparison of predicted heat transfer mechanism components from the correlation developed by Mahmoud and Karayiannis [56].

that was a consistent feature across all flow patterns. Consequently, nucleate boiling is seen to contribute to the heat transfer rates in all observed flow patterns. The study also found that greater pressure drops at lower system pressures resulted in lower fluid temperatures further down the channel. While the heat transfer coefficient was unaffected by mass flux, the fluid temperature decreased, leading to slightly lower wall temperatures. However, this effect was not overly significant.

The correlation by Mahmoud and Karayiannis provided the most accurate predictions among those tested, largely due to its incorporation of the Cooper correlation, which accounts for nucleate boiling effects. This correlation's accuracy confirms the critical role of nucleate boiling in microscale flow boiling scenarios for the investigated fluid and test section surface characteristics, where traditional models may overlook such effects. The success of this model underscores its applicability for predictive purposes in microscale flow boiling, offering a valuable tool for designing efficient heat exchangers and cooling solutions in small-scale systems.

Author statement

T. G. Karayiannis planned the project. Joseph Widgington designed the test section and commissioned the original experimental facility under the supervision of T.G. Karayiannis. A. Ivanov contributed to the project methodology and supervision. Joseph Widgington carried out the experiments and presented the results and first draft for changes and additions to T.G. Karayiannis. All authors discussed the results and contributed to the final manuscript.

CRediT authorship contribution statement

Joseph J. Widgington: Writing – review & editing, Writing – original draft, Visualization, Validation, Methodology, Investigation, Formal analysis, Data curation. **Atanas Ivanov:** Writing – review & editing, Supervision, Project administration, Methodology, Funding acquisition. **Tassos G. Karayiannis:** Writing – review & editing, Writing – original draft, Visualization, Validation, Supervision, Resources, Project administration, Methodology, Investigation, Funding acquisition, Formal analysis, Data curation, Conceptualization.

Declaration of competing interest

The authors declare that they have no known competing financial interests or personal relationships that could have appeared to influence the work reported in this paper.

Acknowledgements

The support of the Engineering and Physical Sciences Research Council (EPSRC) through grant EP/T033045/1 is acknowledged.

The authors would also like to thank Mr. Costas Xanthos for his help in the design and construction of the experimental facility.

Data availability

Data will be made available on request.

References

[1] T.G. Karayiannis, M.M. Mahmoud, Flow boiling in microchannels: fundamentals and applications, Appl. Therm. Eng. 115 (Mar. 2017) 1372–1397, https://doi.org/10.1016/J.APPLTHERMALENG.2016.08.063.
[2] S.G. Kandlikar, History, advances, and challenges in liquid flow and flow boiling heat transfer in microchannels: a critical review, J. Heat Transf. 134 (3) (Mar. 2012), https://doi.org/10.1115/1.4005126/455500.
[3] A. Radwan, M. Ahmed, Thermal management of concentrator photovoltaic systems using microchannel heat sink with nanofluids, Sol. Energy 171 (Sep. 2018) 229–246, https://doi.org/10.1016/J.SOLENER.2018.06.083.
[4] J.R. Thome, A. Cioncolini, Flow boiling in microchannels, Adv. Heat Transf. 49 (2017) 157–224, https://doi.org/10.1016/BS.AIHT.2017.06.001.
[5] G.F. Hewitt, Gas-liquid flow, A-to-Z Guide Thermodyn. Heat Mass Transf. Fluids Eng. (Jul. 2011), https://doi.org/10.1615/ATOZ.G.GAS-LIQUID_FLOW.
[6] G. Hewitt and D.N. Roberts, "Studies of two-phase flow patterns by simultaneous X-ray and flash photography," 1969.
[7] J. Collier, J. Thome, Convective Boiling and Condensation, Oxford University Press, New York, 1994. Accessed: Jan. 08, 2022. [Online]. Available: https://books.google.co.uk/books/about/Convective_Boiling_and_Condensation.html?id=B-1mFnS6UV4C&redir_esc=y.
[8] Y. Taitel, Flow pattern transition in two phase flow, in: 9th International Heat Transfer Conference, Jerusalem, Israel, Aug. 1990, pp. 237–254.
[9] D. Barnea, O. Shoham, Y. Taitel, A.E. Dukler, Flow pattern transition for gas-liquid flow in horizontal and inclined pipes. Comparison of experimental data with theory, Int. J. Multiph. Flow 6 (3) (Jun. 1980) 217–225, https://doi.org/10.1016/0301-9322(80)90012-9.

[10] H.S. Han, W.B. Jeong, M.S. Kim, Frequency characteristics of the noise of R600a refrigerant flowing in a pipe with intermittent flow pattern, Int. J. Refrig. 34 (6) (Sep. 2011) 1497–1506, https://doi.org/10.1016/J.IJREFRIG.2011.04.004.

[11] S. Saini, J. Thaker, J. Banerjee, Transition of stratified-wavy flow to intermittent flow pattern: nonlinear analysis of pressure fluctuations, Lect. Notes Mech. Eng. (2021) 35–46, https://doi.org/10.1007/978-981-33-4684-0_5/COVER.

[12] J.S. Hernandez, C. Valencia, N. Ratkovich, C.F. Torres, F. Muñoz, Data driven methodology for model selection in flow pattern prediction, Heliyon 5 (11) (Nov. 2019), https://doi.org/10.1016/J.HELIYON.2019.E02718 e02718.

[13] A. Arabi, A. Azzi, R. Kadi, A. Al-Sarkhi, B. Hewakandamby, Empirical modelization of intermittent gas/liquid flow hydrodynamic parameters: the importance of distinguishing between plug and slug flows, SPE Prod. Oper. 36 (03) (Aug. 2021) 703–720, https://doi.org/10.2118/205481-PA.

[14] A. Arabi, Y. Salhi, A. Bouderbal, Y. Zenati, E.K. Si-Ahmed, J. Legrand, Onset of intermittent flow: visualization of flow structures, Oil Gas Sci. Technol. – Rev. IFP Energ. nouv. 76 (2021) 27, https://doi.org/10.2516/OGST/2021009.

[15] R. Amaya-Gomez, et al., Probabilistic approach of a flow pattern map for horizontal, vertical, and inclined pipes, Oil Gas Sci. Technol. – Rev. IFP Energ. nouv. 74 (2019) 67, https://doi.org/10.2516/OGST/2019034.

[16] M.M. Mahmoud, T.G. Karayiannis, Flow pattern transition models and correlations for flow boiling in mini-tubes, Exp. Therm. Fluid Sci. 70 (Jan. 2016) 270–282, https://doi.org/10.1016/j.expthermflusci.2015.09.023.

[17] A.H. Al-Zaidi, M.M. Mahmoud, T.G. Karayiannis, Flow boiling of HFE-7100 in microchannels: experimental study and comparison with correlations, Int. J. Heat Mass Transf. 140 (Sep. 2019) 100–128, https://doi.org/10.1016/j.ijheatmasstransfer.2019.05.095.

[18] T.G. Karayiannis, M.M. Mahmoud, Flow boiling in microchannels: fundamentals and applications, Appl. Therm. Eng. 115 (Mar. 2017) 1372–1397, https://doi.org/10.1016/j.applthermaleng.2016.08.063.

[19] Y. Zhang, H. Tan, Y. Li, S. Shan, Y. Liu, A modified heat transfer correlation for flow boiling in small channels based on the boundary layer theory, Int. J. Heat Mass Transf. 132 (Apr. 2019) 107–117, https://doi.org/10.1016/J.IJHEATMASSTRANSFER.2018.11.148.

[20] J.C. Chen, Correlation for boiling heat transfer to saturated fluids in convective flow, Ind. Eng. Chem. Process Des. Dev. 5 (3) (Jul. 1966) 322–329, https://doi.org/10.1021/I260019A023/ASSET/I260019A023.FP.PNG_V03.

[21] J. Lee, I. Mudawar, Two-phase flow in high-heat-flux micro-channel heat sink for refrigeration cooling applications: part II—heat transfer characteristics, Int. J. Heat Mass Transf. 48 (5) (Feb. 2005) 941–955, https://doi.org/10.1016/J.IJHEATMASSTRANSFER.2004.09.019.

[22] S.M. Kim, I. Mudawar, Review of two-phase critical flow models and investigation of the relationship between choking, premature CHF, and CHF in micro-channel heat sinks, Int. J. Heat Mass Transf. 87 (Aug. 2015) 497–511, https://doi.org/10.1016/J.IJHEATMASSTRANSFER.2015.04.012.

[23] Z. Zhang, G. Zhang, Y. Zhang, M. Tian, Experimental study on the effect of hydraulic diameter on the flow boiling characteristics in microchannels, Int. J. Heat Mass Transf. 241 (May 2025) 126736, https://doi.org/10.1016/J.IJHEATMASSTRANSFER.2025.126736.

[24] Y.F. Li, G.D. Xia, D.D. Ma, J.L. Yang, W. Li, Experimental investigation of flow boiling characteristics in microchannel with triangular cavities and rectangular fins, Int. J. Heat Mass Transf. 148 (Feb. 2020) 119036, https://doi.org/10.1016/J.IJHEATMASSTRANSFER.2019.119036.

[25] A.H. Al-Zaidi, M.M. Mahmoud, A. Ivanov, T.G. Karayiannis, Bubble nucleation site density, generation frequency and departure diameter in flow boiling of HFE-7100, Int. J. Heat Mass Transf. 242 (Jun. 2025) 126830, https://doi.org/10.1016/J.IJHEATMASSTRANSFER.2025.126830.

[26] S. Paul, M. Fernandino, C.A. Dorao, On the scaling of convective boiling heat transfer coefficient, Int. J. Heat Mass Transf. 164 (Jan. 2021) 120589, https://doi.org/10.1016/J.IJHEATMASSTRANSFER.2020.120589.

[27] M.M. Mahmoud, T.G. Karayiannis, Flow boiling in mini to microdiameter channels. Encyclopedia of Two-Phase Heat Transfer and Flow IV, World Scientific Publishing, 2018.

[28] S.G. Kandlikar, A general correlation for saturated two-phase flow boiling heat transfer inside horizontal and vertical tubes, J. Heat Transf. 112 (1) (Feb. 1990) 219–228, https://doi.org/10.1115/1.2910348.

[29] Y. Madhour, J. Olivier, E. Costa-Patry, S. Paredes, B. Michel, J.R. Thome, Flow boiling of R134a in a multi-microchannel heat sink with hotspot heaters for energy-efficient microelectronic CPU cooling applications, IEEE Trans. Compon. Packag. Manuf. Technol. 1 (6) (Jun. 2011) 873–883, https://doi.org/10.1109/TCPMT.2011.2123895.

[30] H.L.S.L. Leão, F.J. do Nascimento, G. Ribatski, Flow boiling heat transfer of R407C in a microchannels based heat spreader, Exp. Therm. Fluid Sci. 59 (Nov. 2014) 140–151, https://doi.org/10.1016/J.EXPTHERMFLUSCI.2014.03.014.

[31] W. Qu, I. Mudawar, Flow boiling heat transfer in two-phase micro-channel heat sinks–I. Experimental investigation and assessment of correlation methods, Int. J. Heat Mass Transf. 46 (15) (Jul. 2003) 2755–2771, https://doi.org/10.1016/S0017-9310(03)00041-3.

[32] B. Agostini, J.R. Thome, M. Fabbri, B. Michel, D. Calmi, U. Kloter, High heat flux flow boiling in silicon multi-microchannels – Part I: heat transfer characteristics of refrigerant R236fa, Int. J. Heat Mass Transf. 51 (21–22) (Oct. 2008) 5400–5414, https://doi.org/10.1016/J.IJHEATMASSTRANSFER.2008.03.006.

[33] P.S. Lee, S.V. Garimella, Saturated flow boiling heat transfer and pressure drop in silicon microchannel arrays, Int. J. Heat Mass Transf. 51 (3–4) (Feb. 2008) 789–806, https://doi.org/10.1016/J.IJHEATMASSTRANSFER.2007.04.019.

[34] P. Balasubramanian, S.G. Kandlikar, Experimental study of flow patterns, pressure drop, and flow instabilities in parallel rectangular minichannels, Heat Transf. Eng. 26 (3) (Apr. 2005) 20–27, https://doi.org/10.1080/01457630590907167.

[35] V.Y.S. Lee, G. Henderson, A. Reip, T.G. Karayiannis, Flow boiling characteristics in plain and porous coated microchannel heat sinks, Int. J. Heat Mass Transf. 183 (Feb. 2022) 122152, https://doi.org/10.1016/J.IJHEATMASSTRANSFER.2021.122152.

[36] Ralph. Remsburg, Thermal Design of Electronic Equipment, CRC Press, 2001.

[37] W.M. Kays, A.L. London, Compact Heat Exchangers, 3rd ed., Krieger Publishing, 1960 https://doi.org/10.1115/1.3644004, 1998.

[38] R.J. Phillips, Forced-convection, liquid-cooled, Microchannel Heat Sinks, Massachusetts Institute of Technology, Cambridge, MA, USA, 1987.

[39] B. Markal, O. Aydin, M. Avci, Effect of aspect ratio on saturated flow boiling in microchannels, Int. J. Heat Mass Transf. 93 (Feb. 2016) 130–143, https://doi.org/10.1016/j.ijheatmasstransfer.2015.10.024.

[40] R.D. Blevins, Applied Fluid Dynamics Handbook, Van Nostrand Reinhold Co., New York, N.Y., USA, 1984.

[41] D. Chisholm, Two-phase flow in bends, Int. J. Multiph. Flow 6 (4) (Aug. 1980) 363–367, https://doi.org/10.1016/0301-9322(80)90028-2.

[42] R.K.(Ramesh K.) Shah, A.L.(Alexander L. London, Laminar Flow Forced Convection in ducts : a Source Book For Compact Heat Exchanger Analytical Data, 1st ed., Academic Press, New York, 1978.

[43] H.W. Coleman, W.G. Steele, Experimentation, Validation, and Uncertainty Analysis For Engineers: Third Edition, John Wiley and Sons, 2009, https://doi.org/10.1002/9780470485682.

[44] F.P. Incorpera, D.P. DeWitt, T.L. Bergman, A.S. Lavine, *Incropera's Principles of heat and mass transfer , 1st edition*, Global Edition (2017). Accessed: Jun. 07, 2021. [Online]. Available: https://www.wiley.com/en-gb/Incropera%27s+Principles+of+Heat+and+Mass+Transfer%2C+1st+Edition%2C+Global+Edition-p-9781119409090.

[45] P.X. Jiang, M.H. Fan, G.S. Si, Z.P. Ren, Thermal–hydraulic performance of small scale micro-channel and porous-media heat-exchangers, Int. J. Heat Mass Transf. 44 (5) (Mar. 2001) 1039–1051, https://doi.org/10.1016/S0017-9310(00)00169-1.

[46] P.S. Lee, S.V. Garimella, Thermally developing flow and heat transfer in rectangular microchannels of different aspect ratios, CTRC Res. Publ. 49 (17–18) (Feb. 2006) 3060–3067, https://doi.org/10.1016/j.ijheatmasstransfer.2006.02.011.

[47] Y.Y. Hsu, On the size range of active nucleation cavities on a heating surface, J. Heat Transf. 84 (3) (Aug. 1962) 207–213, https://doi.org/10.1115/1.3684339.

[48] Mirmanto, Single-Phase Flow and Flow Boiling of Water in Horizontal Rectangular Microchannels, Brunel University London, London, UK, 2013.

[49] E.M. Fayyadh, M.M. Mahmoud, K. Sefiane, T.G. Karayiannis, Flow boiling heat transfer of R134a in multi microchannels, Int. J. Heat Mass Transf. 110 (2017) 422–436, https://doi.org/10.1016/J.IJHEATMASSTRANSFER.2017.03.057.

[50] S.S. Bertsch, E.A. Groll, S.V. Garimella, Effects of heat flux, mass flux, vapor quality, and saturation temperature on flow boiling heat transfer in microchannels, Int. J. Multiph. Flow 35 (2) (Feb. 2009) 142–154, https://doi.org/10.1016/J.IJMULTIPHASEFLOW.2008.10.004.

[51] V. Lee, Flow Boiling of HFE-7200 in Multi-Microchannel Heat Sinks for High-Heat Flux Applications, Brunel University London, London, 2020. PhD.

[52] S.M. Kim, I. Mudawar, Review of databases and predictive methods for heat transfer in condensing and boiling mini/micro-channel flows, Int. J. Heat Mass Transf. 77 (Oct. 2014) 627–652, https://doi.org/10.1016/J.IJHEATMASSTRANSFER.2014.05.036.

[53] S. Wang, X. Bi, S. Wang, Boiling heat transfer in small rectangular channels at low reynolds number and mass flux, Exp. Therm. Fluid Sci. 77 (Oct. 2016) 234–245, https://doi.org/10.1016/j.expthermflusci.2016.04.022.

[54] M.M. Shah, Chart correlation for saturated boiling heat transfer: equations and further study, ASHRAE Trans. 88 (Jan. 1982) 185–195. Accessed: Aug. 19, 2021. [Online]. Available: https://inis.iaea.org/search/search.aspx?orig_q=RN:16045958.

[55] G.R. Warrier, V.K. Dhir, L.A. Momoda, Heat transfer and pressure drop in narrow rectangular channels, Exp. Therm. Fluid Sci. 26 (1) (Apr. 2002) 53–64, https://doi.org/10.1016/S0894-1777(02)00107-3.

[56] M.M. Mahmoud, T.G. Karayiannis, Heat transfer correlation for flow boiling in small to micro tubes, Int. J. Heat Mass Transf. 66 (Nov. 2013) 553–574, https://doi.org/10.1016/J.IJHEATMASSTRANSFER.2013.07.042.

[57] J.C. Chen, Correlation for boiling heat transfer to saturated fluids in convective flow, Ind. Eng. Chem. Process Des. Dev. 5 (3) (Jul. 1966) 322–329, https://doi.org/10.1021/I260019A023/ASSET/I260019A023.FP.PNG_V03.

[58] M.G. Cooper, Heat flow rates in saturated nucleate pool boiling-A wide-ranging examination using reduced properties, Adv. Heat Transf. 16 (C) (Jan. 1984) 157–239, https://doi.org/10.1016/S0065-2717(08)70205-3.

[59] G. Criscuolo, W.B. Markussen, K.E. Meyer, M.R. Kærn, High heat flux flow boiling of R1234yf, R1234ze(E) and R134a in high aspect ratio microchannels, Int. J. Heat Mass Transf. 186 (May 2022) 122215, https://doi.org/10.1016/J.IJHEATMASSTRANSFER.2021.122215.

[60] Z. Anwar, B. Palm, R. Khodabandeh, Flow boiling heat transfer and dryout characteristics of R152a in a vertical mini-channel, Exp. Therm. Fluid Sci. 53 (Feb. 2014) 207–217, https://doi.org/10.1016/J.EXPTHERMFLUSCI.2013.12.009.

[61] M. Asim, et al., Flow boiling heat transfer characteristics of low global, Therm. Sci. 26 (1A) (2022) 63–76, https://doi.org/10.2298/TSCI200601327A.

[62] X. Li, L. Jia, The investigation on flow boiling heat transfer of R134a in micro-channels, J. Therm. Sci. 24 (5) (Oct. 2015) 452–462, https://doi.org/10.1007/S11630-015-0808-9/METRICS.
[63] P. Thiangtham, et al., An experimental study on two-phase flow patterns and heat transfer characteristics during boiling of R134a flowing through a multi-microchannel heat sink, Int. J. Heat Mass Transf. 98 (Jul. 2016) 390–400, https://doi.org/10.1016/J.IJHEATMASSTRANSFER.2016.02.051.
[64] M.M. Shah, Unified correlation for heat transfer during boiling in plain mini/micro and conventional channels, Int. J. Refrig. 74 (Feb. 2017) 604–624, https://doi.org/10.1016/j.ijrefrig.2016.11.023.